Computer Physics Communications 328 (2026) 110321

Contents lists available at ScienceDirect

Computer Physics Communications

journal homepage: www.elsevier.com/locate/cpc

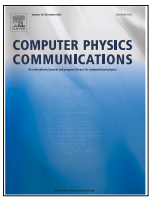

Computational Physics

A Navier-Stokes-peridynamics hybrid algorithm for the coupling of compressible flows and fracturing materials

Mingshuo Han [a,b,1], Shiwei Hu [a,1], Tianbai Xiao [a,c,*], Yonghao Zhang [a,c,*]

[a] Centre for Interdisciplinary Research in Fluids, Institute of Mechanics, Chinese Academy of Sciences, Beijing, 100190, China
[b] Department of Modern Mechanics, University of Science and Technology of China, Hefei, 230027, China
[c] School of Engineering Science, University of Chinese Academy of Sciences, Beijing, 100049, China

ARTICLE INFO

Editor: Andrew Hazel

Keywords:
Peridynamics
Computational fluid dynamics
Fluid-structure interaction
Immersed boundary method
Gas-kinetic scheme

ABSTRACT

Modeling and simulation of fluid-structure interactions are crucial to the success of aerospace engineering. This work addresses a novel hybrid algorithm that models the close coupling between compressible flows and deformable materials using a mesoscopic approach. Specifically, the high-speed flows are described by the gas-kinetic scheme, which is a robust Navier-Stokes solver built on the molecular kinetic theory. The deformation, damage, and fracture of materials are depicted using the bond-based peridynamics, which serves as coarse-grained molecular dynamics to construct non-local extensions of classical continuum mechanics. The evolution of fluids and materials are closely coupled using the ghost-cell immersed boundary method. Within each time step, the solutions of flow and solid fields are updated simultaneously, and physics-driven boundary conditions are exchanged for each other via ghost cells. Extensive numerical experiments, including crack propagation in a pre-cracked plate, subsonic flow around the NACA0012 airfoil, supersonic flow around the circular cylinder, and shock wave impacting on the elastic panel, are performed to validate the algorithm. The simulation results demonstrate the unique advantages of current hybrid algorithm in solving fracture propagation induced by high-speed flows.

1. Introduction

The design of next-generation aerospace vehicles, characterized by long endurance and high maneuverability, necessitates a deep understanding of multi-physics evolution under extreme conditions [1]. Among others, fluid-structure interaction (FSI) represents a key challenge in multi-physics coupling. As the flight envelope expands into high-speed and high-altitude regimes, the mechanism of interaction becomes highly nonlinear. The enhanced compressibility leads to complex flow structures, which cause difficulties in accurate evaluation of aerodynamic stress and heating loads acted on the airframe. The loads can induce structural deformation, material degradation, and even catastrophic fracture, which in turn violently affect the flow evolution. Accurate modeling and simulation of fluid-structure interactions are the key to the success of aerospace engineering [2,3].

To simulate FSI problems, a common strategy is to combine Computational Fluid Dynamics (CFD) with Computational Solid Mechanics (CSM) methods. Strategies typically fall into two categories: boundary-conforming methods (e.g., Arbitrary Lagrangian-Eulerian, ALE) and fixed-grid methods (e.g., Immersed Boundary Method, IBM). While ALE methods track interface movement explicitly [4,5], they face inherent difficulties in handling topological changes caused by severe deformation or fragmentation, often necessitating computationally expensive remeshing. Conversely, the IBM [6–8] simplifies the fluid discretization by modeling boundary effects on a stationary Eulerian grid. This non-conforming flexibility has promoted extensive applications in both rigid [9–12] and flexible body dynamics [13–16] interacting with various flow regimes, ranging from incompressible [17–20] to compressible flows [21–26].

Despite the versatility of IBM-based FSI solvers, simulating flow-induced structural fracture remains a formidable bottleneck. This difficulty stems largely from the continuum-based nature of the traditional Finite Element Method (FEM). Based on partial differential equations (PDEs), FEM faces inherent mathematical singularities when handling spatial discontinuities like cracks. Although remedial techniques such as element deletion, remeshing [27,28], or the Extended Finite Element Method (XFEM) [29,30] have been proposed, they often incur significant computational overhead and algorithmic complexity, particularly when tracking multiple branching cracks in three dimensions.

* Corresponding authors.
E-mail addresses: txiao@imech.ac.cn (T. Xiao), yonghao.zhang@imech.ac.cn (Y. Zhang).
[1] These authors contributed equally to this work.

https://doi.org/10.1016/j.cpc.2026.110321
Received 9 December 2025; Received in revised form 16 July 2026; Accepted 21 July 2026
Available online 24 July 2026

Table 1
Nomenclature.

FSI	fluid-structure interaction
GKS	gas-kinetic scheme
BBPD	bond-based Peridynamics
t, $\mathbf{x}$	time and space variables
$\mathbf{v}$, ζ	particle velocity and internal energy variables
f	particle distribution function
Q	collision operator in the kinetic equation
g	Maxwellian equilibrium distribution function
τ	relaxation time
ρ, $\mathbf{V}$, T, λ	primitive flow variables
$\mathbf{P}$, $\mathbf{q}$	stress tensor and heat flux
ψ	collision invariants
$\mathbf{W}$	conservative flow variables
ρ_s	solid density
$\mathbf{u}$	displacement
δ	horizon radius
$\mathbf{f}$	force density vector
$\mathbf{b}$	body density vector
$\boldsymbol{\xi}$, $\boldsymbol{\eta}$	relative position and displacement vectors
ω	micropotential
s	bond stretch
c	micromodule function
$\bar{\mathbf{W}}$	cell-averaged conservative variables
$\mathbf{F}^W$	numerical fluxes for conservative variables
$\Delta\mathbf{S}$	area vector of cell faces
g_0, f_0	initial equilibrium and non-equilibrium distributions in GKS
a, b, A	normal, tangential, and temporal derivatives in GKS
ν, β	volume and surface effect correction factors
GC	ghost cell
IBM	immersed boundary method
IP	imaginary point
BI	boundary intersection
$\mathbf{n}_s$	outward unit normal vector at boundary

Peridynamics (PD), a non-local theory of continuum mechanics proposed by Silling [31], offers a paradigm shift for fracture modeling. By replacing the spatial derivatives in PDEs with integral equations, PD circumvents the issue of undefined derivatives at discontinuities. It models material behavior through non-local interactions between material points, allowing damage and fracture to emerge spontaneously as part of the solution process without requiring external crack tracking algorithms. Silling et al. [32], Zhang et al. [33], Oterkus et al. [34], Madenci and Oterkus [35], Zhang et al. [36] Over the past two decades, PD has proven robust in capturing complex failure modes, including crack branching and fragmentation [37–44].

Recognizing the potential of Peridynamics in handling structural discontinuities, researchers have explored its integration with various fluid solvers. Continuum-based solvers, such as Isogeometric Analysis (IGA) [45,46], have been employed to model blast or aerodynamic loading. Furthermore, the direct-forcing IBM has been utilized to study material failure under prescribed flow fields [47]. Distinct from these approaches, due to the shared mesoscopic characteristics, Lattice Boltzmann Methods (LBM) have been frequently coupled with PD to simulate fluid-driven deformation in incompressible regimes [48]. However, notwithstanding this methodological diversity, a unifying limitation characterizes the current state of the art: these studies predominantly focus on incompressible or weakly compressible flows, or rely on simplified one-way coupling mechanisms. As the flow enters the high-speed compressible regime, the distinct wave propagation characteristics (e.g., shock-structure interference) and the strict conservation requirements pose new challenges that previous incompressible frameworks cannot adequately address.

This work aims to bridge this gap by establishing a novel, closely coupled framework tailored for compressible flow-induced fracture. Distinguished from traditional macroscopic continuum solvers, we adopt a mesoscopic perspective for both fluid and solid phases. For the fluid, we employ the Gas-Kinetic Scheme (GKS) [49–51], a robust Navier-Stokes solver based on the Boltzmann equation, which excels in capturing sharp shock discontinuities and viscous stresses. For the solid, the bond-based Peridynamics describes the material response and failure. The coupling is achieved via a ghost-cell immersed boundary method, ensuring accurate exchange of momentum and energy across the moving, potentially fracturing interface. By unifying the kinetic description of fluids and the particle-based description of solids, this hybrid algorithm provides a high-fidelity tool for analyzing the catastrophic interaction between shock waves and fracturing structures.

The rest of the paper is structured as follows. Section 2 briefly introduces basic theories of compressible fluids and fracturing materials. Section 3 presents the formulation of the solution algorithm and its detailed implementations. Section 5 includes numerical experiments to demonstrate the performance of the current method. The last section presents concluding remarks. The nomenclature is presented in Table 1.

2. Theory of fluids and solids

2.1. Gas kinetic theory

Gas kinetic theory provides an insightful perspective for understanding non-equilibrium fluid transport and designing numerical schemes that are compatible with entropy-increasing processes. The Boltzmann equation and its simplified models describe the evolution of a many-particle system statistically based on the single-particle distribution function. The Boltzmann-BGK model [52] takes the form

$$\partial_t f + \mathbf{v}\cdot\nabla_{\mathbf{x}} f = Q(f) = \frac{g-f}{\tau}, \tag{1}$$

where $f(t,\mathbf{x},\mathbf{v},\zeta)$ is the particle distribution function with respect to time, space, velocity, and internal energy modes. The collision operator is denoted by Q, where τ is the collision time and g is the Maxwellian that corresponds to thermodynamic equilibrium state, i.e.

$$g = \rho\Big(\frac{\lambda}{\pi}\Big)^{\frac{N+3}{2}} \exp\left[-\lambda\big((\mathbf{v}-\mathbf{V})^2+\zeta^2\big)\right], \tag{2}$$

where ρ is the density, N is the number of internal degrees of freedom, $\mathbf{V}$ is the macroscopic velocity, and $\lambda = m/2kT$, with m being the molecular mass, k the Boltzmann constant, and T the temperature. The degrees of freedom of internal energy takes $(5-3\gamma)/(\gamma-1)+1$, where γ is the adiabatic index. The internal variable in the equilibrium is thus given by $\zeta^2 = \zeta_1^2+\cdots+\zeta_N^2$. Note that the BGK model provides the fixed Prandtl number $\mathrm{Pr}=1$. This deficiency can be ameliorated by correcting the equilibrium distribution in Eq. (1), e.g., the Shakhov [53] and ES-BGK models [54].

The conservative variables can be derived by taking the moments of the distribution function over the velocity space, i.e.,

$$\mathbf{W} = \begin{pmatrix}\rho\\ \rho\mathbf{V}\\ \rho E\end{pmatrix} = \int \psi f \, d\Xi, \tag{3}$$

where E denotes the total energy density, ψ is the vector of collision invariants,

$$\psi = \Big(1, \mathbf{v}, \tfrac{1}{2}(\mathbf{v}^2+\zeta^2)\Big)^T, \tag{4}$$

and $d\Xi = d\mathbf{v}d\zeta$.

It is known that the Euler and Navier-Stokes equations can be derived as the limits of solutions of the Boltzmann equation. Considering the first-order Chapman-Enskog expansion of f, i.e.,

$$f = g + f_1 = g - \tau(\partial_t g + \mathbf{v}\cdot\nabla_{\mathbf{x}} g), \tag{5}$$

we can take conservative moments of the BGK equation, which yields

$$\int \psi(\partial_t g + \mathbf{v}\cdot\nabla_{\mathbf{x}} g)d\Xi = \tau\int \psi(\partial_t f_1 + \mathbf{v}\cdot\nabla_{\mathbf{x}} f_1)d\Xi, \tag{6}$$

from which the Navier-Stokes equations can be obtained, i.e.,

$$\begin{aligned}
&\frac{\partial \rho}{\partial t} + \nabla_{\mathbf{x}} \cdot (\rho \mathbf{V}) = 0, \\
&\frac{\partial \rho \mathbf{V}}{\partial t} + \nabla_{\mathbf{x}} \cdot (\rho \mathbf{V} \otimes \mathbf{V}) - \nabla_{\mathbf{x}} \cdot \mathbf{P} = 0, \\
&\frac{\partial \rho E}{\partial t} + \nabla_{\mathbf{x}} \cdot (\rho E \mathbf{V}) - \nabla_{\mathbf{x}} \cdot (\mathbf{P} \cdot \mathbf{V}) + \nabla_{\mathbf{x}} \cdot \mathbf{q} = 0,
\end{aligned} \tag{7}$$

where $\otimes$ denotes dyadic product. The stress tensor and heat flux are defined as

$$\mathbf{P} = \int_{\mathbb{R}^3} (\mathbf{v} - \mathbf{V}) \otimes (\mathbf{v} - \mathbf{V}) f \, d\mathbf{v}, \quad \mathbf{q} = \int_{\mathbb{R}^3} \frac{1}{2} (\mathbf{v} - \mathbf{V})(\mathbf{v} - \mathbf{V})^2 f \, d\mathbf{v}. \tag{8}$$

Inserting Eq. (5) into the above equation gives the Newton's stress formula and Fourier's law, which naturally recovers the Navier-Stokes equations.

In the context of viscosity-dominated flows, the collision time τ is linked to the dynamic viscosity μ through the relation $\tau = \mu/p$. Conversely, for heat-conduction-dominated flows, the collision time is selected as $\tau = \kappa/c_p p$ to recover the heat conduction coefficient κ.

The Chapman-Enskog expansion provides a comprehensive and consistent description of equilibrium (inviscid Euler) and non-equilibrium (viscous) effects in the Navier-Stokes equations. No artificial assumptions other than the truncation order are made. A family of gas-kinetic schemes (GKS) [55–57] have been developed based on the evolutionary Chapman-Enskog solution within the framework of BGK equation. In this work, the GKS solver is employed to solve the evolution of compressible flows, see Section 3.1 for details.

2.2. Peridynamic theory

Peridynamics is explicitly formulated based on Newton's second law of motion. The governing equation of bond-based Peridynamic (BBPD) can be written as

$$\rho_s(\mathbf{x}) \ddot{\mathbf{u}}(t, \mathbf{x}) = \int_{H_{\mathbf{x}}} \mathbf{f}(\mathbf{u}' - \mathbf{u}, \mathbf{x}' - \mathbf{x}) dV' + \mathbf{b}(t, \mathbf{x}), \tag{9}$$

where $\rho_s(\mathbf{x})$ denotes the mass density of solid at the position $\mathbf{x}$. The displacement is denoted as $\mathbf{u}$, and thus $\ddot{\mathbf{u}}$ is the acceleration vector field. The force density vector between the particles $\mathbf{f}$ is a function of the relative position $\mathbf{x}' - \mathbf{x}$ and the relative displacement $\mathbf{u}' - \mathbf{u}$. The body force density vector is denoted as $\mathbf{b}$. The interactions between particles are modeled through integrals over the domain of influence. The integral domain (also known as horizon) is defined,

$$H_{\mathbf{x}} = \{\mathbf{x}' \in \mathbb{R} : |\mathbf{x} - \mathbf{x}'| < \delta\}, \tag{10}$$

where δ is the radius of horizon. The volume occupied by the particle at $\mathbf{x}'$ is denoted as V'. After the configuration deformation, we denote the new positions of the particles as $\mathbf{y}'$ and $\mathbf{y}$, where $\mathbf{y}' = \mathbf{x}' + \mathbf{u}'$ and $\mathbf{y} = \mathbf{x} + \mathbf{u}$. We introduce $\boldsymbol{\xi}$ and $\boldsymbol{\eta}$ to represent the relative position and displacement vectors between the particles $\mathbf{x}$ and $\mathbf{x}'$, where $\boldsymbol{\xi} = \mathbf{x}' - \mathbf{x}$ and $\boldsymbol{\eta} = \mathbf{u}' - \mathbf{u}$. As shown in Fig. 1, $\boldsymbol{\xi}$ denotes the reference bond between two particles in the initial configuration. The deformed bond in the deformed configuration is represented by the vector sum $\boldsymbol{\xi} + \boldsymbol{\eta}$.

For a microelastic material [31], a pairwise potential ω can be modeled such that

$$\mathbf{f}(\boldsymbol{\eta}, \boldsymbol{\xi}) = \frac{\partial \omega(\boldsymbol{\eta}, \boldsymbol{\xi})}{\partial \boldsymbol{\eta}}, \quad \forall \boldsymbol{\xi}, \boldsymbol{\eta}. \tag{11}$$

Under simple linear microelasticity, the micropotential is defined as

$$\omega(\boldsymbol{\eta}, \boldsymbol{\xi}) = \frac{c s^2 \|\boldsymbol{\xi}\|}{2}, \tag{12}$$

where c represents the micromodule function, and s represents the bond stretch, i.e.,

$$s = \frac{\|\boldsymbol{\xi} + \boldsymbol{\eta}\| - \|\boldsymbol{\xi}\|}{\|\boldsymbol{\xi}\|}. \tag{13}$$

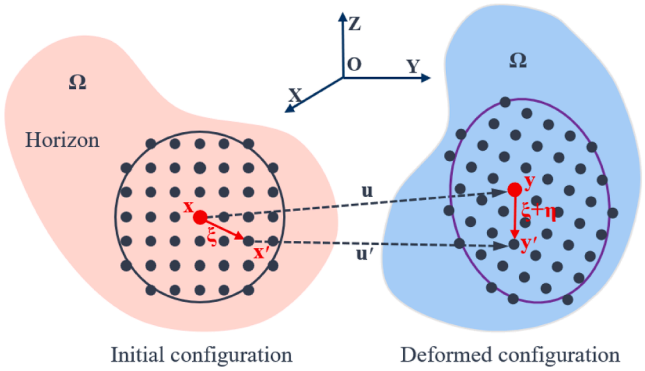

Fig. 1. Illustration of BBPD and pairwise interaction between PD points. The horizon of the particle at the position $\mathbf{x}$ encompasses all the PD particles interacting with it, and remains unchanged throughout deformation.

Therefore, the corresponding pairwise force $\mathbf{f}$ becomes

$$\mathbf{f}(\boldsymbol{\eta}, \boldsymbol{\xi}) = \frac{\partial \omega(\boldsymbol{\eta}, \boldsymbol{\xi})}{\partial \boldsymbol{\eta}} = c s \|\boldsymbol{\xi}\| \frac{\partial s}{\partial \boldsymbol{\eta}} = c s \frac{\boldsymbol{\xi} + \boldsymbol{\eta}}{\|\boldsymbol{\xi} + \boldsymbol{\eta}\|}. \tag{14}$$

Here, the micromodule function c takes usually the constant form as

$$c = \begin{cases} \dfrac{2E}{\pi \delta^2 A}, & \text{for 1D,} \\ \dfrac{9E}{\pi \delta^3 h}, & \text{for plane stress,} \\ \dfrac{48E}{5\pi \delta^3 h}, & \text{for plane strain,} \\ \dfrac{12E}{\pi \delta^4}, & \text{for 3D.} \end{cases} \tag{15}$$

It should be noted that although the GKS solver naturally accounts for the total energy evolution in the fluid domain, the PD formulation in Eq. (9) is treated as purely mechanical. This approximation is justified by significant disparity between the characteristic speeds of stress wave propagation and thermal diffusion. In this study, the structural response is driven by stress waves traveling at the longitudinal wave speed $c_L = \sqrt{E/\rho}$. Concurrently, the thermal influence propagates at a diffusion speed, where the heat penetration depth over a characteristic time t is estimated as $\delta_T \sim \sqrt{\alpha t}$. For the millisecond-scale events investigated here, the ratio of the thermal affected zone to the mechanical deformation zone is infinitesimal, i.e., $\delta_T \ll c_L t$. Consequently, the thermal gradients remain confined to a thin skin layer near the fluid-solid interface, and their coupling effect on the global stress field and crack trajectory is secondary. Thus, the mechanical response can be accurately decoupled from the thermal conduction process.

Failure of functional materials can be naturally formulated in the BBPD since it allows a bond to break when its stretch exceeds a predefined threshold. The tensile force in the bond is no longer sustained after the failure. Therefore, we modify the bond force density as

$$\mathbf{f} = \lambda_s c s \frac{\boldsymbol{\xi} + \boldsymbol{\eta}}{\|\boldsymbol{\xi} + \boldsymbol{\eta}\|}. \tag{16}$$

Here, λ_s is a history-dependent scalar valued function that describes the state of bond failure. When the bond stretch s exceeds the critical bond stretch s_c, the bond state are set to zero, i.e.,

$$\lambda_s = \begin{cases} 1.0, & \text{if } s < s_c, \\ 0.0, & \text{if } s \geq s_c. \end{cases} \tag{17}$$

The critical bond stretch s_c can be determined by the material's critical energy release rate G_c [58], i.e.,

$$s_c = \begin{cases} \sqrt{\dfrac{\pi G_c}{3k\delta}} & \text{for 2D,} \\ \sqrt{\dfrac{5G_c}{9k\delta}} & \text{for 3D,} \end{cases} \tag{18}$$

where k is the bulk modulus of the material.

Despite its advantages in handling discontinuities, the BBPD is mathematically constrained by a fixed Poisson's ratio. Specifically, for isotropic materials, the BBPD is limited to $\nu = 0.25$ in three-dimensional cases and $\nu = 1/3$ for two-dimensional plane stress conditions. This intrinsic restriction limits its applicability to a broader range of engineering materials.

3. Solution algorithm

3.1. Gas-kinetic scheme

The gas-kinetic scheme is a finite volume method. The computational domain $\mathbf{\Omega}$ is divided into N_x non-overlapping elements, and the cell-averaged conservative variables are introduced as

$$\bar{\mathbf{W}}_i = \frac{1}{V_i}\int_{\mathbf{\Omega}_i} \mathbf{W}(t,\mathbf{x})d\mathbf{x}. \tag{19}$$

Integrating Eq. (7) yields the update algorithm of $\bar{\mathbf{W}}$, i.e.,

$$\frac{\partial \bar{\mathbf{W}}_i}{\partial t} = -\frac{1}{V_i}\oint_{\partial\mathbf{\Omega}_i} \mathbf{F}^W \cdot d\mathbf{S} = -\frac{1}{V_i}\sum_{k=1}^{N_f} \mathbf{F}_k^W \cdot \Delta\mathbf{S}_k, \tag{20}$$

where $\mathbf{F}^W$ denotes the numerical fluxes, $\mathbf{S} = \mathbf{n}\Delta S$ is the area vector pointing out of the cell, and N_f is the number of faces.

The core task in the finite volume method is to accurately compute the numerical fluxes. For brevity, we employ the two-dimensional Cartesian coordinate system to introduce the principle of gas-kinetic flux solver. It can be straightforwardly extended to non-orthogonal mesh using local coordinate transformation.

Under the assumption that the collision time is a local constant, the integral solution of the BGK equation in Eq. (1) at a cell face $(x_{i+1/2}, y_j)$ writes

$$\begin{aligned} f(x_{i+1/2},y_j,t,u,v,\zeta) = {} & \frac{1}{\tau}\int_0^t g(x',y',t',u,v,\zeta)e^{-(t-t')/\tau}dt' \\ & + e^{-t/\tau} f_0(x_{i+1/2}-ut, y_j - vt), \end{aligned} \tag{21}$$

where $x' = x_{i+1/2} - u(t-t')$, $y' = y_j - v(t-t')$ are the particle trajectories, f_0 is the initial distribution function at the beginning of each time step ($t = 0$). Two unknowns g and f_0 are constructed to concretize the above equation and construct the numerical fluxes. We assume, without loss of generality, that $x_{i+1/2} = 0$ and $y_j = 0$ to simplify the notation.

The initial distribution function is constructed following the piecewise Chapman-Enskog expansion, i.e.,

$$f_0 = \begin{cases} g^l\left(1 + a^l x + b^l y - \tau(a^l u + b^l v + A^l)\right), & x \le 0 \\ g^r(1 + a^r x + b^r y - \tau(a^r u + b^r v + A^r)), & x > 0 \end{cases} \tag{22}$$

where g^l and g^r are the Maxwellian distributions related to the left and right-hand states around a face, while $\{a^l, a^r\}$ and $\{b^l, b^r\}$ are related to the slopes in the normal and tangential directions. The explicit forms of these derivatives can be found in [55].

The equilibrium state is constructed as

$$g = g_0(1 + (1 - H(x))\bar{a}^l x + H(x)\bar{a}^r x + \bar{b}y + \bar{A}t), \tag{23}$$

where g_0 is the initial Maxwellian distribution at the face, while $\{\bar{a}^l, \bar{a}^r\}$ and $\bar{b}$ are connected with the normal and tangential slopes of g. The $H(x)$ is the heaviside step function,

$$H(x) = \begin{cases} 0, & \text{if } x < 0, \\ 1, & \text{if } x \ge 0. \end{cases} \tag{24}$$

In both f and g, the slopes are related to the gradients of macroscopic variables via

$$\int f a\psi d\Xi = \partial_x \mathbf{W}, \quad \int f b\psi d\Xi = \partial_y \mathbf{W}, \tag{25}$$

and can then be determined by solving a linear system. Substituting Eqs. (22) and (23) yields the time dependent solution at the face,

$$\begin{aligned} f(x_{i+\frac{1}{2}},y_j,t,u,v,\xi) = {} & (1-e^{-t/\tau})g_0 \\ & + \left[\tau(-1+e^{-t/\tau}) + te^{-t/\tau}\right]\left[\bar{a}^l H(u) + \bar{a}^r(1-H(u))\right]ug_0 \\ & + \tau\left(\frac{t}{\tau} - 1 + e^{-t/\tau}\right)\bar{A}g_0 \\ & + e^{-t/\tau}\left[(1-u(t+\tau)\bar{a}^l)H(u)g^l\right. \\ & \left.+(1-u(t+\tau)\bar{a}^r)(1-H(u))g^r\right] \\ & + e^{-t/\tau}\left[-\tau A^l H(u)g^l - \tau A^r(1-H(u))g^r\right]. \end{aligned} \tag{26}$$

The numerical fluxes can thus be computed by

$$\begin{pmatrix} F_\rho \\ F_{\rho U} \\ F_{\rho V} \\ F_{\rho E} \end{pmatrix}_{i+\frac{1}{2},j} = \int u \begin{pmatrix} 1 \\ u \\ v \\ \frac{1}{2}(u^2+v^2+\zeta^2) \end{pmatrix} f\left(x_{i+\frac{1}{2}}, j, t, u, v, \zeta\right) d\Xi. \tag{27}$$

3.2. Peridynamic solver

In the peridynamic solver, the solid region is discretized into a group of material points. The integral operator in Eq. (9) is approximated by the numerical quadrature. The semi-discrete governing equation of the bond-based peridynamics (BBPD) writes

$$\rho_s(\mathbf{x}_i)\ddot{\mathbf{u}}(t,\mathbf{x}_i) = \sum_{j=1}^{N_i}[\mathbf{f}_{i,j}(\mathbf{u}_j - \mathbf{u}_i, \mathbf{x}_j - \mathbf{x}_i)\beta_{i,j}\nu_{i,j}V_j] + \mathbf{b}(t,\mathbf{x}_i), \tag{28}$$

where N_i is the number of particles within the horizon of the particle located at $\mathbf{x}_i$. The subscript j denotes an arbitrary particle positioned at $\mathbf{x}_j$ within the horizon of the particle at $\mathbf{x}_i$, and V_j is the volume of the particle at $\mathbf{x}_j$ within the horizon of the particle at $\mathbf{x}_i$. For the simplest uniform distribution of points, $V_j = (\Delta x_s)^3$. Here, Δx_s represents the particle spacing. $\nu_{i,j}$ and $\beta_{i,j}$ are the correction factors for the volume and surface effects respectively for the particle at $\mathbf{x}_j$ within the horizon of the particle at $\mathbf{x}_i$. The explicit forms of these correction factors can be found in [31].

Based on Eq. (16), the spatially discrete form of the force density vector of each bond $\mathbf{f}_{i,j}$ satisfies

$$\begin{aligned} \mathbf{f}_{i,j}(\mathbf{u}_j - \mathbf{u}_i, \mathbf{x}_j - \mathbf{x}_i) &= cs\lambda_s \frac{\boldsymbol{\xi}_{ij} + \boldsymbol{\eta}_{ij}}{\left|\boldsymbol{\xi}_{ij} + \boldsymbol{\eta}_{ij}\right|} \\ &= c\lambda_s \frac{\left|\boldsymbol{\xi}_{ij} + \boldsymbol{\eta}_{ij}\right| - \left|\boldsymbol{\xi}_{ij}\right|}{\left|\boldsymbol{\xi}_{ij}\right|} \frac{\boldsymbol{\xi}_{ij} + \boldsymbol{\eta}_{ij}}{\left|\boldsymbol{\xi}_{ij} + \boldsymbol{\eta}_{ij}\right|} \\ &= c\lambda_s \frac{\left|\mathbf{y}_j - \mathbf{y}_i\right| - \left|\mathbf{x}_j - \mathbf{x}_i\right|}{\left|\mathbf{x}_j - \mathbf{x}_i\right|} \frac{\mathbf{y}_j - \mathbf{y}_i}{\left|\mathbf{y}_j - \mathbf{y}_i\right|}. \end{aligned} \tag{29}$$

The explicit forward and backward difference scheme is employed as the integrator along the time direction. The dynamic evolution of displacement, velocity, and acceleration is computed as

$$\begin{aligned} \ddot{\mathbf{u}}_i^{(n)} &= \frac{\mathbf{f}_{i,j}^{(n)} + \mathbf{b}^{(n)}(\mathbf{x}_i, n\Delta t)}{\rho(\mathbf{x}_i)}, \\ \dot{\mathbf{u}}_i^{(n+1)} &= \dot{\mathbf{u}}_i^{(n)} + \ddot{\mathbf{u}}_i^{(n)}\Delta t, \\ \mathbf{u}_i^{(n+1)} &= \mathbf{u}_i^{(n)} + \dot{\mathbf{u}}_i^{(n+1)}\Delta t. \end{aligned} \tag{30}$$

3.3. Immersed boundary method

The ghost-cell immersed boundary method (GCIBM) is employed to couple the evolution of the structure and the flow fluid. The schematic of the GCIBM method is shown in Fig. 2. The boundary of the solid is represented by discrete body markers (depicted by purple pentagons)

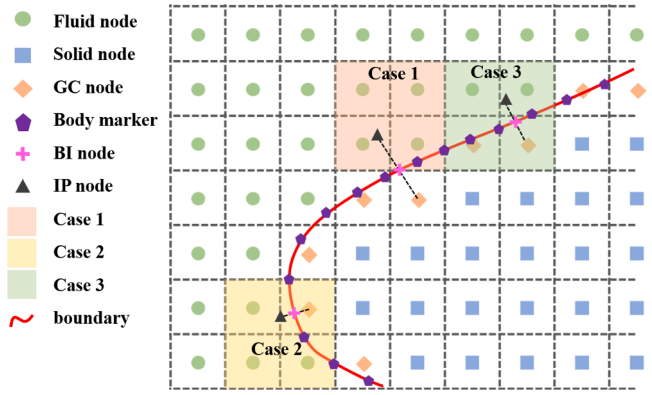

Fig. 2. Schematic showing the GC-related nodes on the 2D fluid-structure boundary.

connected by linear segments, which distinguishes the fluid cells (depicted by green circles) and the solid cells (depicted by blue squares). The ghost cells (depicted by orange diamonds) are virtual points within the solid domain near the fluid-structure interface, facilitating the application of boundary conditions. Imaginary point (IP) nodes (depicted by black triangles) are symmetrically located across the boundary relative to the GC nodes, while boundary intersection (BI) nodes (depicted by magenta plus signs) are defined as the midpoints between the GC and their corresponding IP nodes.

The key to GCIBM lies in calculating the pseudo flow variables in the GCs, which play a dual role in the simulation. On one hand, they are integral to flow simulation by enforcing the no-slip and no-penetration boundary conditions. On the other hand, variables defined at GCs, e.g., pressure, are used to compute the forces exerted on the solid boundary, which in turn serve as boundary conditions for PD, which is crucial for capturing fluid-structure interactions.

3.3.1. Identification of imaginary points and boundary intersections

The boundary of the solid body is represented by a set of discrete BMs, which are pre-defined as a subset of the PD nodes located on the structural surface. The connectivity of these BMs is established in a prescribed counter-clockwise sequence to form a series of line segments. In each coupling cycle, the positions of the BMs are updated by synchronizing them with the latest coordinates of their corresponding PD nodes. For a given GC, the corresponding boundary segment is identified as the one with the minimum distance to the GC center. Subsequently, the location of IP and nodes can be determined via

$$\mathbf{x}_{\mathrm{IP}} = \mathbf{x}_{\mathrm{GC}} + 2d\mathbf{n}_{\mathrm{s}}, \quad \mathbf{x}_{\mathrm{BI}} = \frac{\mathbf{x}_{\mathrm{IP}} + \mathbf{x}_{\mathrm{GC}}}{2}, \tag{31}$$

where $\mathbf{x}_{\mathrm{GC}}$, $\mathbf{x}_{\mathrm{IP}}$, and $\mathbf{x}_{\mathrm{BI}}$ are the positions of the GC, IP, and BI nodes, respectively. Here, d is the distance from the GC to the corresponding boundary segment, and $\mathbf{n}_{\mathrm{s}}$ is the outward unit normal vector of that specific segment, calculated based on the updated BM coordinates.

3.3.2. Calculation of variables at boundary intersections

The BI nodes are typically positioned between boundary nodes (with possible overlap). The variables at the BI nodes can be computed using the Lagrange interpolation,

$$\phi_{\mathrm{BI}} = \frac{(x_{\mathrm{BI}} - x_2)(y_{\mathrm{BI}} - y_2)}{(x_1 - x_2)(y_1 - y_2)}\phi_1 + \frac{(x_1 - x_{\mathrm{BI}})(y_1 - y_{\mathrm{BI}})}{(x_1 - x_2)(y_1 - y_2)}\phi_2, \tag{32}$$

where (x_1, y_1) and (x_2, y_2) denote the two neighboring boundary nodes.

3.3.3. Calculation of variables at imaginary points

The bi-linear interpolation method is used to compute any flow variable ϕ (e.g., pressure, velocity, and temperature) at the IP node. Such interpolation technique utilizes the information from the nearest neighboring fluid cells around the IP. The variables ϕ at the IP are expressed as

$$\phi = w_1 + w_2 x_{\mathrm{IP}} + w_3 y_{\mathrm{IP}} + w_4 x_{\mathrm{IP}} y_{\mathrm{IP}}, \tag{33}$$

where w_i $(i = 1, 2, 3, 4)$ are the interpolation coefficients, determined by the following Eqs. (34)–(38) based on the indices of the neighboring fluid nodes.

If all four neighboring nodes are fluid nodes (Case 1 in Fig. 2), the coefficients w_i are determined by:

$$\begin{bmatrix} w_1 \\ w_2 \\ w_3 \\ w_4 \end{bmatrix} = \begin{bmatrix} 1 & x_1 & y_1 & x_1 y_1 \\ 1 & x_2 & y_2 & x_2 y_2 \\ 1 & x_3 & y_3 & x_3 y_3 \\ 1 & x_4 & y_4 & x_4 y_4 \end{bmatrix}^{-1} \begin{bmatrix} \phi_1 \\ \phi_2 \\ \phi_3 \\ \phi_4 \end{bmatrix}, \tag{34}$$

where $\{x_i, y_i\}_{i=1,2,3,4}$ represents the locations of four neighboring fluid nodes around the IP, respectively.

If one of the four nodes belongs to the solid domain (Case 2 in Fig. 2), the BI node replaces the solid node in the interpolation. Given the Dirichlet fluid-solid boundary condition, the coefficients w_i are calculated as

$$\begin{bmatrix} w_1 \\ w_2 \\ w_3 \\ w_4 \end{bmatrix} = \begin{bmatrix} 1 & x_1 & y_1 & x_1 y_1 \\ 1 & x_2 & y_2 & x_2 y_2 \\ 1 & x_3 & y_3 & x_3 y_3 \\ 1 & x_{\mathrm{BI}} & y_{\mathrm{BI}} & x_{\mathrm{BI}} y_{\mathrm{BI}} \end{bmatrix}^{-1} \begin{bmatrix} \phi_1 \\ \phi_2 \\ \phi_3 \\ \phi_{\mathrm{BI}} \end{bmatrix}, \tag{35}$$

where $(x_{\mathrm{BI}}, y_{\mathrm{BI}})$ and ϕ_{BI} represent the coordinates and interpolated values at the BI point, respectively. Given the Neumann-type boundary condition, where the flux is specified as $\hat{\mathbf{n}} \cdot \nabla\phi = h$, the bi-linear interpolation weights w_i $(i = 1, 2, 3, 4)$ are computed by:

$$\begin{bmatrix} w_1 \\ w_2 \\ w_3 \\ w_4 \end{bmatrix} = \begin{bmatrix} 1 & x_1 & y_1 & x_1 y_1 \\ 1 & x_2 & y_2 & x_2 y_2 \\ 1 & x_3 & y_3 & x_3 y_3 \\ 0 & n_{x,\mathrm{BI}} & n_{y,\mathrm{BI}} & x_{\mathrm{BI}} n_{y,\mathrm{BI}} + y_{\mathrm{BI}} n_{x,\mathrm{BI}} \end{bmatrix}^{-1} \begin{bmatrix} \phi_1 \\ \phi_2 \\ \phi_3 \\ h \end{bmatrix}, \tag{36}$$

where $\hat{\mathbf{n}} = (n_{x,\mathrm{BI}}, n_{y,\mathrm{BI}})$ is the unit normal vector at the BI node, and $n_{x,\mathrm{BI}}$ and $n_{y,\mathrm{BI}}$ are its components along the x and y directions.

If two of the four nodes belong to the solid domain (Case 3 in Fig. 2), the boundary intersection points (BI1 and BI2) replace the two solid nodes. Under the Dirichlet boundary condition, the interpolation coefficients w_i are determined by

$$\begin{bmatrix} w_1 \\ w_2 \\ w_3 \\ w_4 \end{bmatrix} = \begin{bmatrix} 1 & x_1 & y_1 & x_1 y_1 \\ 1 & x_2 & y_2 & x_2 y_2 \\ 1 & x_{\mathrm{BI1}} & y_{\mathrm{BI1}} & x_{\mathrm{BI1}} y_{\mathrm{BI1}} \\ 1 & x_{\mathrm{BI2}} & y_{\mathrm{BI2}} & x_{\mathrm{BI2}} y_{\mathrm{BI2}} \end{bmatrix}^{-1} \begin{bmatrix} \phi_1 \\ \phi_2 \\ \phi_{\mathrm{BI1}} \\ \phi_{\mathrm{BI2}} \end{bmatrix}, \tag{37}$$

where $(x_{\mathrm{BI1}}, y_{\mathrm{BI1}})$, $(x_{\mathrm{BI2}}, y_{\mathrm{BI2}})$, ϕ_{BI1}, and ϕ_{BI2} represent the coordinates and interpolated variables at the two BI points. For the Neumann-type boundary condition, where the fluxes at BI1 and BI2 are specified as g_1 and g_2, respectively, the interpolation coefficients are computed by

$$\begin{bmatrix} w_1 \\ w_2 \\ w_3 \\ w_4 \end{bmatrix} = \begin{bmatrix} 1 & x_1 & y_1 & x_1 y_1 \\ 1 & x_2 & y_2 & x_2 y_2 \\ 0 & n_{x1,\mathrm{BI1}} & n_{y1,\mathrm{BI1}} & x_{\mathrm{BI1}} n_{y,\mathrm{BI1}} + y_{\mathrm{BI1}} n_{x1,\mathrm{BI1}} \\ 0 & n_{x2,\mathrm{BI2}} & n_{y2,\mathrm{BI2}} & x_{\mathrm{BI2}} n_{y,\mathrm{BI2}} + y_{\mathrm{BI2}} n_{x2,\mathrm{BI2}} \end{bmatrix}^{-1} \begin{bmatrix} \phi_1 \\ \phi_2 \\ g_1 \\ g_2 \end{bmatrix}. \tag{38}$$

The obtained interpolation weights w_i are then used to compute the variables at the IP nodes using Eq. (33).

3.3.4. Calculation of variables in ghost cells

Once the variables at the IP and BI nodes are determined corresponding to the given boundary conditions, the variables in the ghost cells can be calculated. For an arbitrary variable ϕ, governed by the Dirichlet boundary condition, the variables at GC nodes are calculated as

$$\phi_{\mathrm{GC}} = 2\phi_{\mathrm{BI}} - \phi_{\mathrm{IP}}. \tag{39}$$

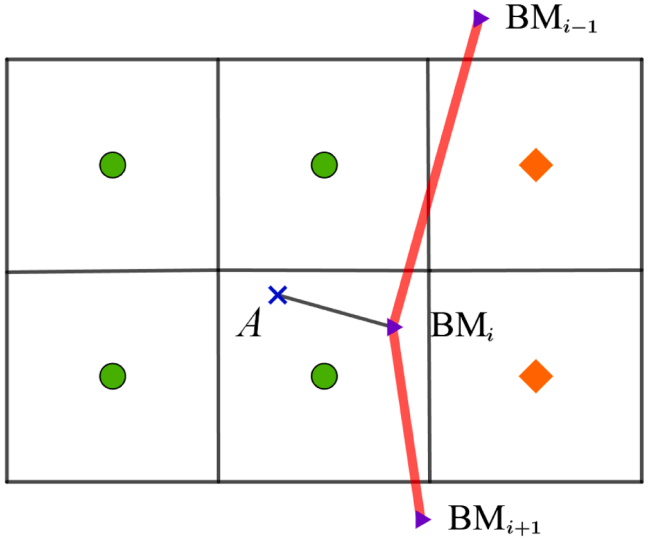

Fig. 3. The solution algorithm of fluid-structure coupling.

For pressure p, which is governed by the Neumann boundary condition, the status in the GC is given by $p_{\mathrm{GC}} = p_{\mathrm{BI}}$. And thus, using the ideal gas law, the density at the GC nodes is computed as

$$\rho_{\mathrm{GC}} = \frac{p_{\mathrm{GC}}}{RT_{\mathrm{GC}}}, \tag{40}$$

where R is the gas constant.

3.3.5. Calculation of Peridynamics' boundary condition

In order to impose the fluid loading on the solid, the pressure on the boundary must be evaluated accurately. In this work, the pressure on each body marker is obtained using a bi-linear interpolation of the surrounding fluid cells.

As illustrated in Fig. 3, since the pressure satisfies the zero normal gradient condition at the solid boundary, a point A is selected along the outward normal direction to evaluate the boundary pressure. The coordinates of point A are obtained as

$$\mathbf{x}_A = \mathbf{x}_{\mathrm{BM}_i} + l\,\mathbf{n}_s, \tag{41}$$

where $\mathbf{x}_{\mathrm{BM}_i}$ is the coordinate of the ith body marker, and $\mathbf{n}$ is the outward normal vector, approximated by the outward normal of the segment connecting BM_{i-1} and BM_i. The distance l should satisfy

$$l > \frac{\sqrt{2}}{2}\Delta x_s. \tag{42}$$

We choose $l = 0.8\Delta x_s$.

The pressure at A is then obtained using the bi-linear interpolation method described in Section 3.3.3. Because the normal pressure gradient vanishes at the boundary, the pressure at the BM_i point is simply

$$p_{\mathrm{BM}_i} = p_A. \tag{43}$$

Finally, the pressure is converted into a body-force density vector acting on the corresponding PD node via

$$\mathbf{b} = -\frac{1}{\Delta x_s} p\mathbf{n}_s, \tag{44}$$

where Δx_s represents the PD's particle spacing. This provides consistent fluid loading for the PD computation under the immersed boundary method.

The solution algorithm of fluid-structure coupling is summarized in Fig. 4.

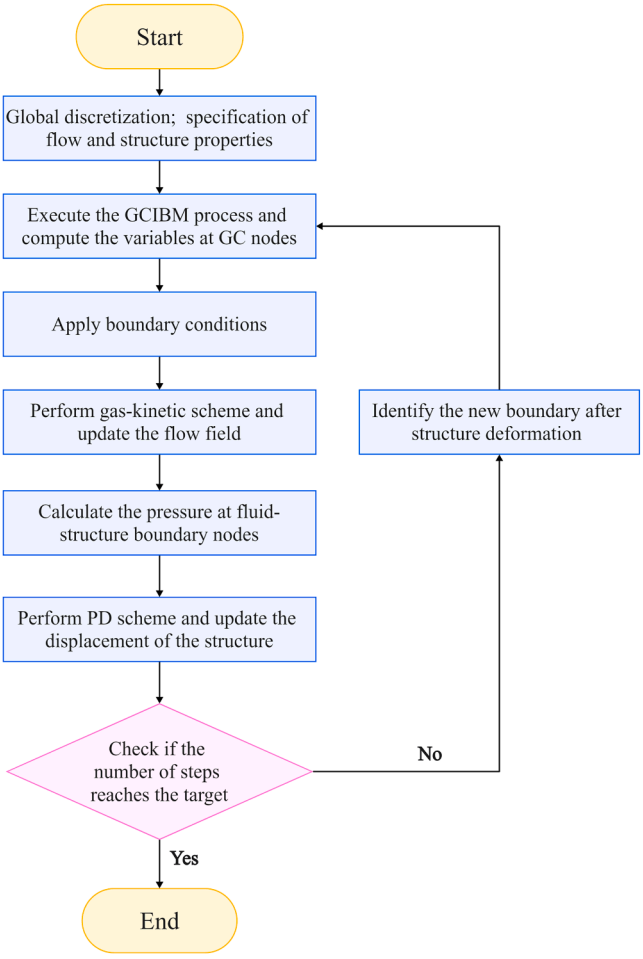

Fig. 4. The solution algorithm of fluid-structure coupling.

Table 2
Comparison of drag coefficient predicted by the current simulations with the reported data.

Method	Body-conformal [59]	IBM [61]	Current Simulation
C_D	1.547	1.525	1.556

Table 3
Fluid properties and flow conditions for the simulation.

Material	Density (kg/m^3)	Pressure (kPa)	Specific Heat Ratio	Velocity (m/s)
Stationary air	1.20	101.0	1.4	0
Inflow air	1.63	155.7	1.4	109.6

Table 4
Comparison of drag coefficient for different mesh resolutions.

Cases	$\Delta x_f = D/100$	$\Delta x_f = D/200$	$\Delta x_f = D/400$	Experimental result [64]
C_{D}	1.3792	1.3865	1.3890	1.3962

3.4. Time-step determination

To ensure the numerical stability of the explicit coupling procedure, a synchronized global time step Δt is employed for both the fluid and solid solvers. At each duty cycle, this time step is determined by the more restrictive of the two stability constraints:

$$\Delta t = \min(\Delta t_{\mathrm{f}}, \Delta t_{\mathrm{s}}), \tag{45}$$

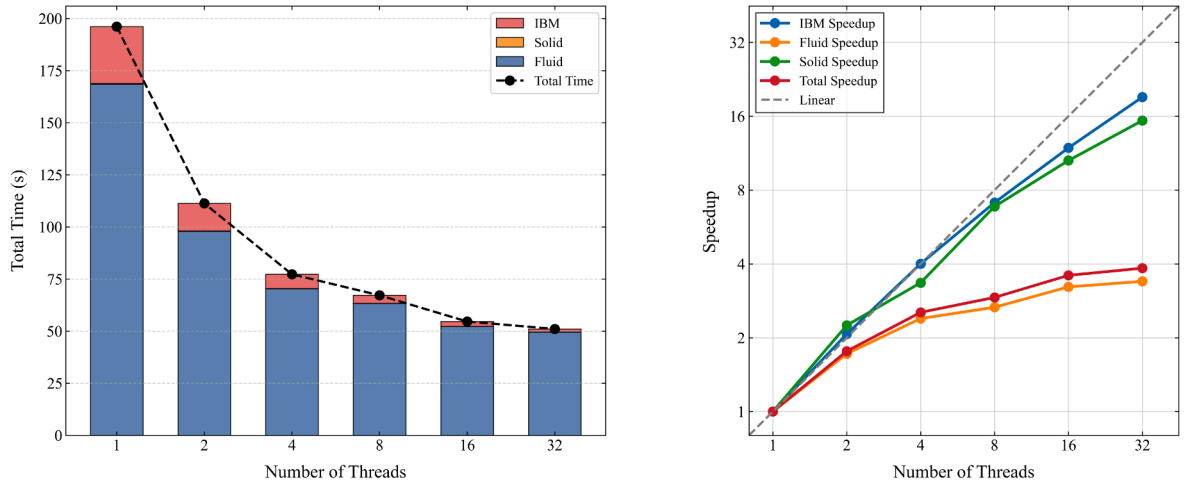

(a) Wall-clock time breakdown per time step (b) Strong scaling speedup curves

Fig. 5. Parallel performance analysis on the AMD EPYC 7763 processor (Fluid grid: 2.56×10^6, Solid mesh: 1.3×10^5). (a) Wall-clock time breakdown per time step. (b) Strong scaling speedup curves.

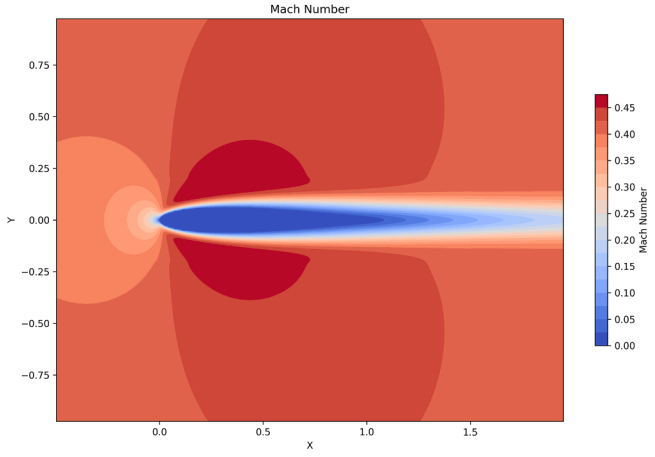

Fig. 6. Mach number distribution in the flow field around the airfoil.

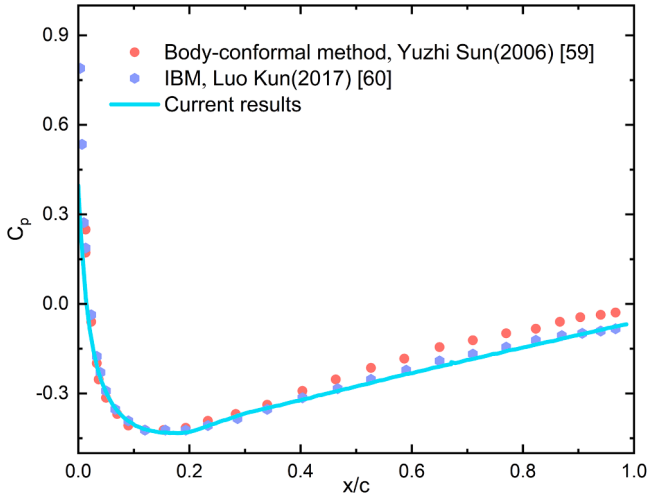

Fig. 7. Comparison of the pressure coefficient distribution C_p along the airfoil surface, where the horizontal axis x/c represents the relative horizontal position along the airfoil, where c is the airfoil chord length, and the vertical axis C_p represents the pressure distribution.

where the first term represents the CFL condition for the GKS fluid solver, and the second term denotes the stability limit for the explicit PD integration [32].

3.5. Spatial accuracy analysis

In the present hybrid framework, the overall spatial accuracy of the GCIBM is determined by two major sources: the geometric approximation error and the interpolation error.

3.5.1. Geometric approximation error

In the GCIBM, linear segments defined by discrete body markers (BM) are employed to represent the boundary of the solid. Consequently, there is a geometric approximation error (often referred to as the sagitta error) between the discrete boundary intersection (BI), $\mathbf{x}_{\text{BI}}$, and the true physical location, $\mathbf{x}_{\text{true}}$. Based on the geometric relationship between the chord and the arc, this error is derived as:

$$|\mathbf{x}_{\text{BI}} - \mathbf{x}_{\text{true}}| \approx R - \sqrt{R^2 - \left(\frac{\Delta s}{2}\right)^2} \approx \frac{\Delta s^2}{8R}, \tag{46}$$

where R is the local curvature radius of the boundary and Δs represents the spacing of BMs. As described in Section 3.3.1, these BMs are predefined as a subset of the PD nodes located on the structural surface, which ensures that the marker spacing Δs is inherently coupled to the particle spacing Δx_s (i.e., $\Delta s \approx \Delta x_s$). Therefore, the geometric approximation error can be expressed as:

$$|\mathbf{x}_{\text{BI}} - \mathbf{x}_{\text{true}}| \approx \frac{\Delta s^2}{8R} \approx \frac{\Delta x_s^2}{8R} = O\left(\frac{\Delta x_s^2}{R}\right). \tag{47}$$

Since the curvature radius typically satisfies $R \gg \Delta x_s$ in smooth regions, the geometric error scales as $O(\Delta x_s^2)$. However, when $R \sim O(\Delta x_s)$, such as in sharp corners or highly curved regions, the local geometric error degrades to $O(\Delta x_s)$.

3.5.2. Interpolation error

The interpolation accuracy depends on the reconstruction schemes for the IP (Imaginary Point) and the BI nodes, as well as the accuracy of the underlying flow and structure fields.

For the IP node, bi-linear interpolation is adopted, which inherently provides second-order spatial accuracy. Since the GKS solver itself is second-order accurate in space, the interpolation error of flow variables at the IP node remains consistent at $O(\Delta x_f^2)$.

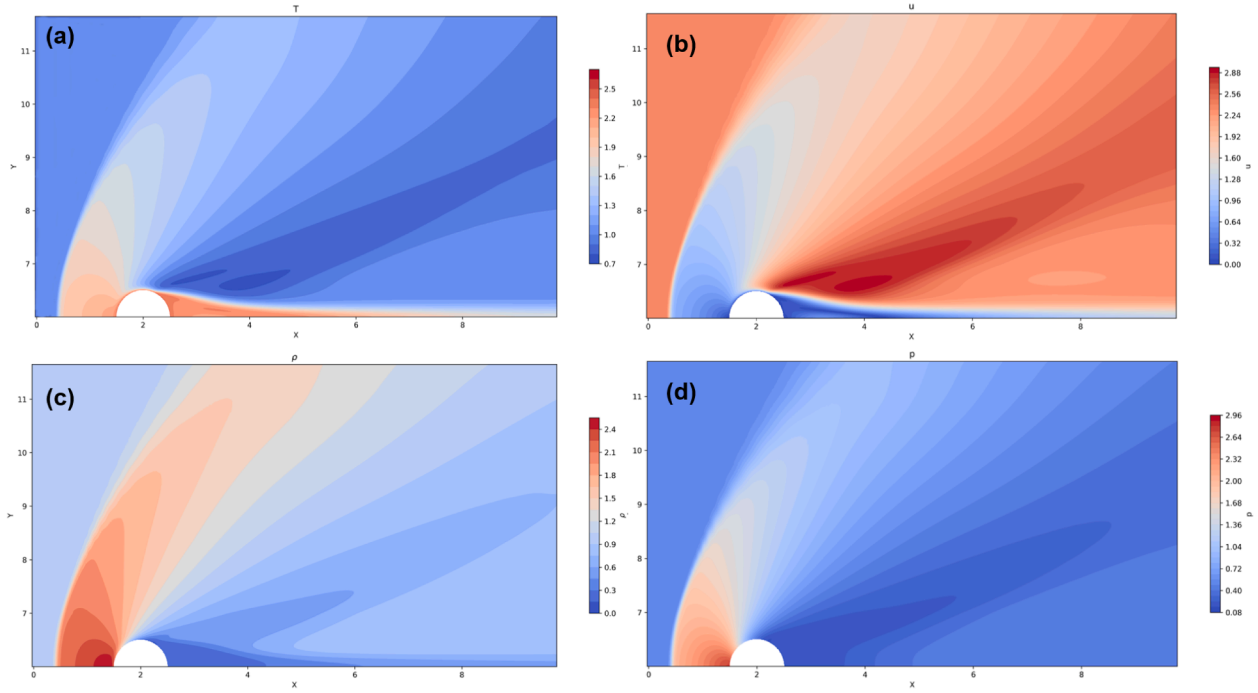

Fig. 8. Distribution of solution fields in the supersonic flow around circular cylinder. (a) temperature; (b) velocity; (c) density; (d) pressure.

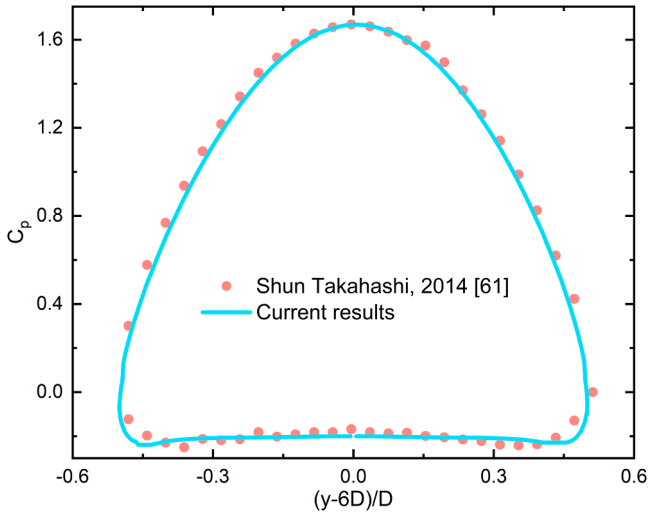

Fig. 9. Comparison of the pressure coefficient distribution C_p along the cylinder surface between the results from the current model and those from the literature. In this figure, the horizontal axis (y-6D)/D represents the relative vertical position along the cylinder, where D is the diameter of the cylinder, and the vertical axis C_p represents the pressure distribution.

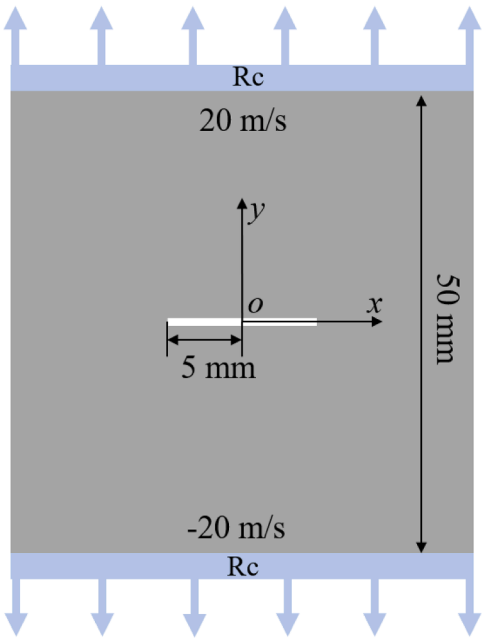

Fig. 10. Schematic of the plate with a pre-existing crack.

For the BI node, the interpolation accuracy is determined by the PD field near the solid boundary. In regions where the deformation is continuous, the displacement and velocity fields are smoothly distributed. Consequently, the truncation error of BI variables reconstructed from the surrounding material nodes is on the order of $O(\Delta x_s^2)$. However, if a discontinuity (e.g., a fracture) is present near the boundary, the stencil may cross the jump in properties, increasing the error to $O(\Delta x_s)$. Thus, the BI interpolation becomes first-order accurate in these areas.

Based on the mirror relation Eq. (39), the overall ghost-cell accuracy follows the lower order of the IP and BI accuracies. Therefore, in continuous boundary regions, the ghost-cell reconstruction maintains second-order spatial accuracy, while in discontinuous regions, the accuracy reduces to first order.

Combining the geometric approximation and interpolation analyses, it can be concluded that the present hybrid framework achieves second-order spatial accuracy in regions where the boundary is smooth and continuous. However, in discontinuous or high-curvature regions, the effective spatial accuracy degrades to the first order.

4. Performance analysis

To evaluate the computational efficiency and scalability of the proposed parallel FSI framework, a strong scaling test was conducted using the cylinder flow benchmark. The fluid domain is defined as a square region $\Omega_f = [-4.0, 4.0] \times [-4.0, 4.0]$ m, discretized by a uniform Cartesian

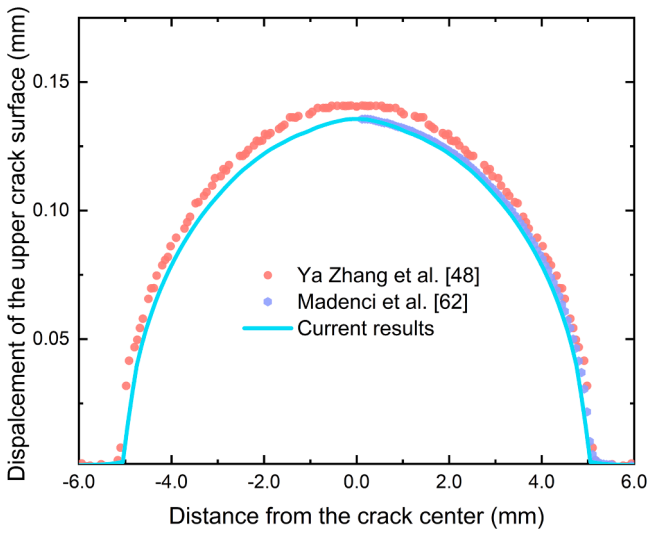

Fig. 11. Vertical displacement of the material points near the upper surface of initial crack at the time t = 16.7 μs when failure is not allowed.

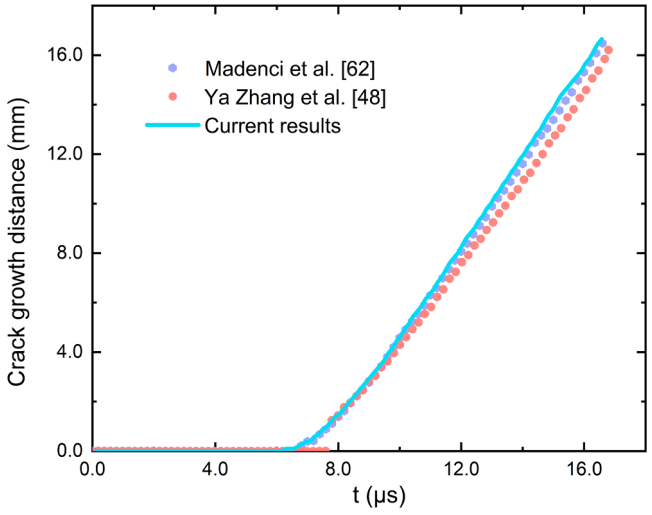

Fig. 12. Variation in the propagation distance of the right crack tip during growth, when failure occurs.

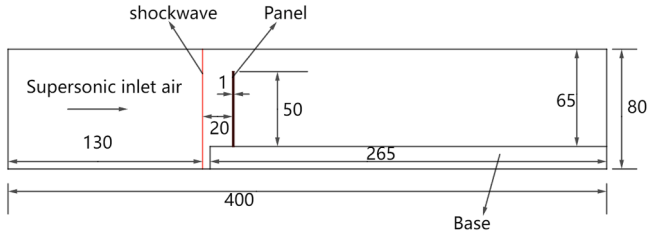

Fig. 13. Schematic of the shock tube experiment.

grid of 1600×1600 cells (Total fluid nodes: 2.56×10^6). The solid cylinder is discretized into approximately 1.3×10^5 Lagrangian elements. The radius of horizon in PD is set to $\delta = 0.02$, and the system time step is fixed at $\Delta t = 8.6 \times 10^{-7}$ s.

The parallelization of the proposed framework is implemented using the native multi-threading capabilities of the Julia language. Specifically, the `@threads` macro is employed to distribute computationally intensive tasks—such as the flux evaluation in the GKS module and the bond force integration in the PD module—across multiple CPU cores. This shared-memory parallelization approach achieves efficient data access and minimal communication overhead.

Benchmarks were performed on an **AMD EPYC 7763 64-Core Processor**. The performance was measured by varying the thread count $N \in \{1, 2, 4, 8, 16, 32\}$. The wall-clock time was averaged over the last 10 steps to ensure statistical stability.

The runtime breakdown and parallel speedup are presented in Fig. 5. The results indicate distinct scaling behaviors arising from the algorithmic nature of each module:

- **Scalability of Solid and Coupling modules:** Both the Peridynamics (PD) solver and the GCIBM coupling module exhibit excellent parallel efficiency (Fig. 5(b)). The particle-based nature of PD allows independent force calculations, ensuring effective load balancing. Similarly, the GCIBM module scales well due to the parallelized identification of ghost cells and flow reconstruction. This ensures that the dynamic boundary treatment does not penalize the overall simulation speed.
- **Saturation of GKS Fluid Solver:** In contrast, the GKS module shows limited scalability. Although the runtime decreases initially, the speedup factor plateaus at approximately 4.0, regardless of further increases in thread count. Consequently, the fluid solver remains the dominant contributor to the total computational cost at high parallel configurations.

The saturation of the total speedup is largely dictated by the performance characteristics of the GKS fluid solver. Two primary factors contribute to this limited scaling: (1) **Memory Bandwidth Constraints:** Unlike standard macroscopic solvers, the reconstruction of distribution functions at cell interfaces in GKS creates a memory-bound process that prevents ideal scaling on shared-memory architectures. As the number of threads increases, the memory bandwidth saturates, limiting the data throughput required for flux calculations; (2) **Complex Stencil Operations:** The multi-dimensional reconstruction and flux splitting in GKS involve complex data dependencies and logic that are less amenable to linear scaling compared to the explicit loops in the PD solver.

Despite the saturation of the fluid solver, the parallel implementation still offers a meaningful performance gain. For typical configurations (e.g., $N = 16$), the proposed method reduces the wall-clock time per step from 196.1 s to 54.6 s, achieving a 3.84× speedup. The reduction in wall-clock time confirms that the parallelization of the computationally intensive solid and coupling parts effectively accelerates the overall FSI simulation.

5. Numerical experiments

5.1. Validation of compressible flow solver

We first validate the gas-kinetic compressible flow solver along with the immersed boundary method. Two benchmark cases are employed as numerical experiments, i.e., the laminar flow around a NACA0012 airfoil and the supersonic flow around a circular cylinder.

5.1.1. Subsonic flow around a NACA0012 airfoil

The NACA0012 airfoil is considered at a zero angle of attack ($\alpha = 0°$), with the freestream Mach number $\mathrm{Ma} = 0.5$ and the Reynolds number $\mathrm{Re} = 5000$. The computational domain spans $(-10D, 20D) \times (-10D, 10D)$, with the leading edge of the airfoil located at the origin.

A non-uniform Cartesian grid is employed. A fine grid ($\Delta x_f = \Delta y_f = D/512$) is used near the airfoil, while a coarser grid ($\Delta x_f = \Delta y_f = D/2$) is applied in more distant areas. At the far-field boundaries, the left boundary is specified with freestream conditions, while the top, bottom, and right boundaries are treated with the zero-gradient extrapolation condition to allow waves to pass through without significant reflection. On the airfoil surface, a no-slip wall boundary condition is applied using GCIBM.

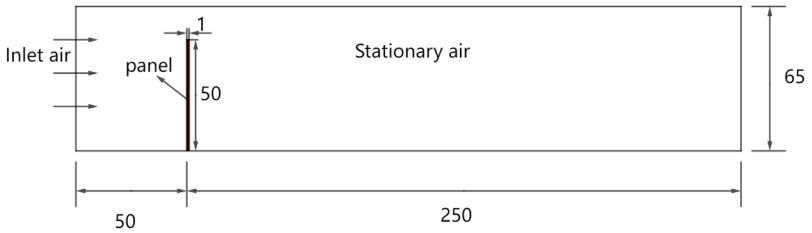

Fig. 14. Simplified geometric configuration for numerical simulation.

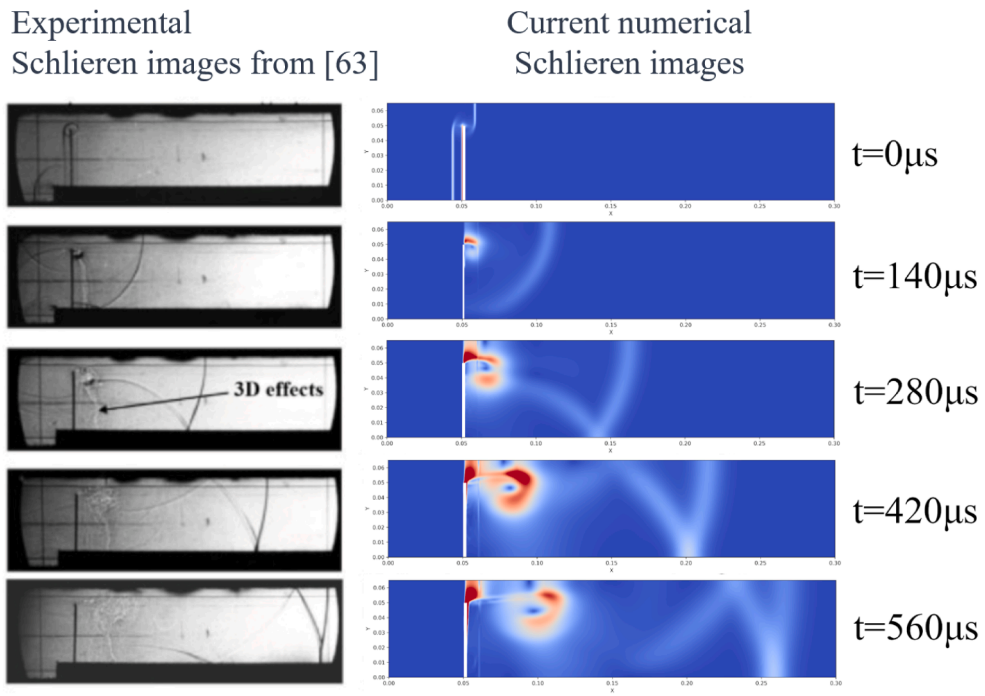

Fig. 15. Comparison between the time evolution of (a) the experimental Schlieren photos from [63] and (b) our numerical results for the panel with 50 mm length.

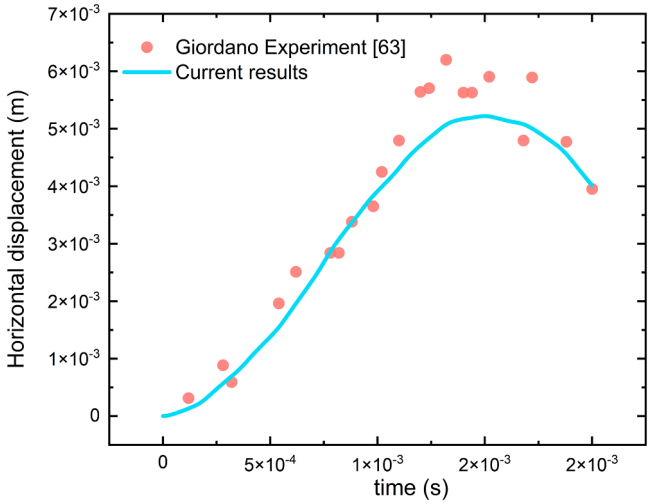

Fig. 16. Variation in the horizontal displacement of the panel end, where the experiment data refer to Giordano [63].

Fig. 6 shows the Mach number distribution around the airfoil. Fig. 7 presents the comparison of the pressure coefficient distribution along the airfoil surface between the current results and those from the literature [59,60]. The consistency between these results confirms the sufficiency of the current approach in accurately predicting viscous compressible flows with boundary effects.

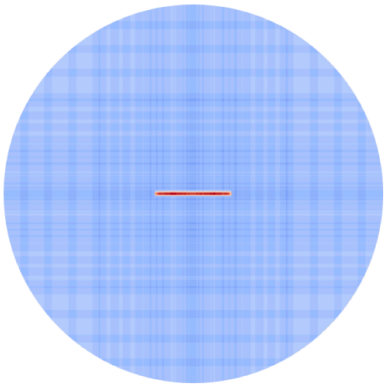

Fig. 17. Pre-existing crack inside the cylinder.

5.1.2. Supersonic flow around a circular cylinder

The supersonic flow around a circular cylinder is considered. The freestream Mach number is set as Ma = 2.0, and the Reynolds number, Re = 300. The computational domain spans $(0,10D) \times (0,12D)$, with the cylinder center located at $(2D,6D)$.

Similar as the airfoil case, a non-uniform grid is employed. A fine grid ($\Delta x_f = \Delta y_f = D/512$) is used near the cylinder surface, while a coarser

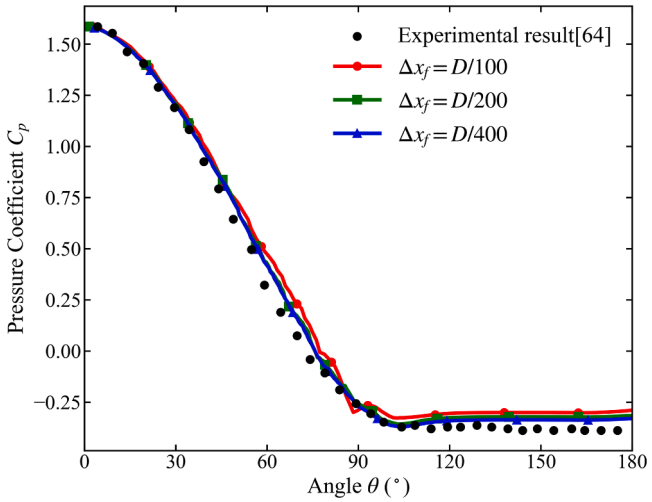

Fig. 18. Comparison of surface pressure coefficient (C_p) distributions along the cylinder for different mesh resolutions, where the experiment data refer to Bashkin [64].

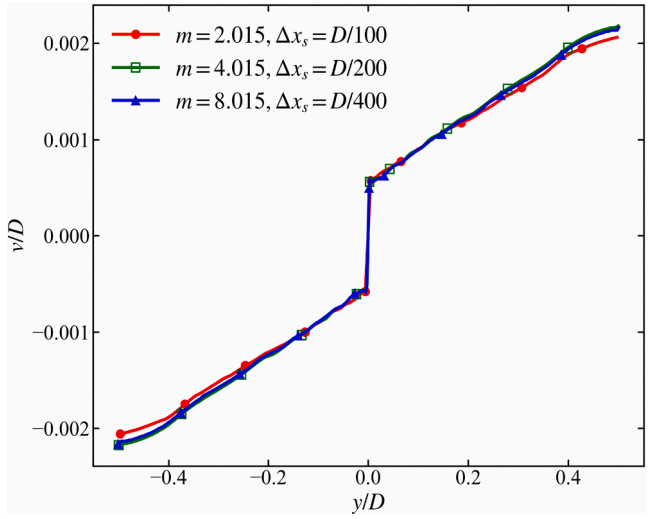

Fig. 19. m-convergence study of the displacement in y-direction along the line $x = 2D$.

grid ($\Delta x_f = \Delta y_f = D/2$) is applied in the distant regions. At the far-field boundaries, the left boundary is specified with freestream conditions, while the top, bottom, and right boundaries are treated with the zero-gradient extrapolation condition to allow waves to pass through without significant reflection. On the cylinder surface, a no-slip wall boundary condition is applied using GCIBM.

Fig. 8 shows the Mach number distribution around the cylinder, and Fig. 9 presents a comparison of the pressure coefficient distribution along the cylinder surface between the results from the current model and those from the literature [61]. The comparison of drag coefficients C_D from different numerical methods is shown in Table 2. The numerical experiments demonstrate that the current approach is capable of accurate prediction of the behavior of supersonic flow as it interacts with solid boundaries.

5.2. Validation of peridynamic solver

We then validate the peridynamic model for structural deformation and crack propagation. A two-dimensional plate with an inherent crack is settled. The plate dimensions are $L = 50\,\text{mm}$ (length) and $W = 50\,\text{mm}$ (width). A horizontal crack of length $D = 10\,\text{mm}$ is initialized at the plate's center. The material is assumed to be isotropic and linear elastic with Young's modulus E of 192 GPa and the density of 8000 kg/m^3.

The plate is discretized into 500×500 material points. The distance between material points is $\Delta x_s = 0.02\,\text{mm}$, and the horizon size is set as $\delta = 3.015\Delta x_s$. The velocity boundary conditions of $u_y = \pm 20\,\text{m/s}$ are applied along its upper and lower edges. Two fictitious boundary layers, R_c, each containing 500×3 material points, are added at the top and bottom to enforce the boundary condition. The simulation employs a time step of $\Delta t = 1.3367 \times 10^{-8}\,\text{s}$. The schematic of the numerical experiment is shown in Fig. 10.

The fracture behavior of the plate is governed by the critical stretch s_c. Fig. 11 presents the comparison of the shape of cracks predicted by the current method and literature results at $s_c = 1.0$. Fig. 12 provides the predicted fracture propagation velocity compared with the reference solution [48,62]. The overall good agreement suggests that the current bond-based Peridynamic solver can describe material deformation and damage.

5.3. Validation of the coupling scheme

Here, the fluid-structure interaction solver is to be validated using the experimental setup by Giordano [63]. The Giordano model features an elastic panel fixed at its lower edge to a rigid base. This setup is placed in a shock tube consisting of a movable high-pressure chamber (0.75 m long), a fixed low-pressure chamber (2.02 m long), and a movable experimental chamber (0.98 m long), as summarized in Fig. 13.

Ning et al. [25] simplified the model by assuming a tube length of 300 mm with a positive shock imposed at the left boundary. The base was removed under the assumption that its impact on the results is negligible. In the simplified model, the panel has a length of 50 mm and a thickness of 1 mm, and its material behavior is linear elastic. The simplified experimental setup is illustrated in Fig. 14. The initial flow field and material parameters are summarized in Table 3. The material of panel is assumed to be isotropic and linear elastic with Young's modulus E of 220 GPa and the density of 7850 kg/m^3.

The computational domain spans $(0, 6L) \times (0, 1.3L)$. To reduce computational cost, a non-uniform grid is used in the x-direction, with finer grid spacing ($\Delta x_f = 0.002L$) near the plane and coarser grid spacing ($\Delta x_f = 0.02L$) farther away. Since the plane length is comparable to the domain size in the y-direction, a uniform grid is adopted in the y-direction, with a grid spacing of $\Delta y_f = 0.02L$. The left boundary is set as a fixed inlet condition based on the inflow air in Table 3, while the right boundary employs a zero-gradient extrapolation condition. The top and bottom boundaries are treated with no-slip wall boundary condition. On the panel surface, a no-slip wall boundary condition is applied using GCIBM.

The panel is discretized into 4×200 material points. The distance between material points is $\Delta x_s = 0.005L$, and the horizon size is set as $\delta = 3.015\Delta x_s$. A fictitious boundary layers containing 4×3 material points is added at the bottom to enforce the fixed boundary condition.

Fig. 15 shows the comparison of the Schlieren images between [63] and our simulation results. Fig. 16 shows the displacement of the panel's end during the loading process over 2 ms, based on both the experimental and current simulation data. The numerical results show good agreement with the experimental data [63]. In the time range from 0 to about 1.5 ms, the displacement increase is consistent with the experimental data. After 1.5 ms, the decrease in displacement also agrees well with the experimental results.

5.4. Fracture inside a cylinder induced by supersonic flow

Finally, we consider a typical supersonic fluid-solid interaction scenario with the flow conditions derived from the experimental studies of Bashkin [64]. In this case, the free stream moving of Mach number 1.7 impacts a cylinder that contains a pre-existing internal crack. Upon

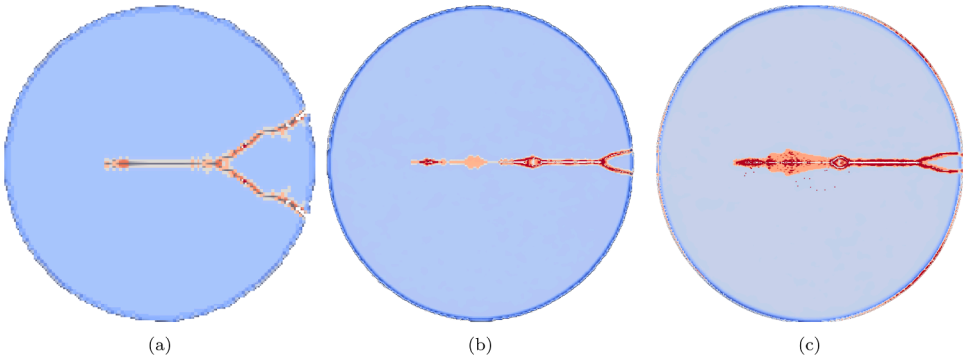

Fig. 20. Crack path computed with differentgrids for a nominal horizon size $\delta = D/50$. (a)$m = 2.015$, $\Delta x_s = D/100$; (b)$m = 4.015$, $\Delta x_s = D/200$, (c)$m = 8.015$, $\Delta x_s = D/400$.

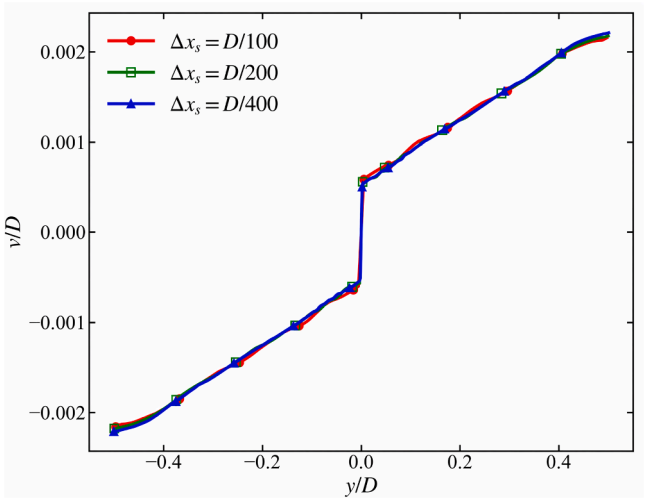

Fig. 21. δ-convergence study of the displacement in y-direction along the line $x = 2D$.

impact, the crack propagates, showcasing the distinct advantages of the current PD-based FSI model.

The supersonic flow with Ma = 1.7 and Re = 200,000 is considered in the simulation. The diameter of the cylinder is $D = 0.024m$. The computational domain spans $(0,10D) \times (0,12D)$, with the cylinder center located at $(2D,6D)$. A non-uniform grid is used with a fine grid near the cylinder and a coarser grid in the distant regions. At the far-field boundaries, the left boundary is specified with freestream conditions, while the top, bottom, and right boundaries are treated with the zero-gradient extrapolation condition to allow waves to pass through without significant reflection. On the cylinder surface, a no-slip wall boundary condition is applied using GCIBM.

The material is assumed to be isotropic and linear elastic with the density of 100 kg/m^3. An initial crack is pre-defined inside the cylinder, as shown in Fig. 17.

5.4.1. Grid convergence studies

To investigate the grid convergence of the FSI response, a systematic refinement study is performed by varying the resolution of the fine grid region near the cylinder. Three sets of grids near the cylinder are considered: $\Delta x_f = D/100, D/200, D/400$. The transition to the coarser far-field grid follows the same stretching ratio across all cases. Correspondingly, the Peridynamic particle spacing Δx_s is adjusted to match the local fluid grid size (i.e. $\Delta x_s = \Delta x_f$) to ensure a consistent spatial discretization at the fluid-solid interface. The material properties of the cylinder are set as follows: the Young's modulus is $E = 25$ MPa, and the critical stretch is $s_c = 0.02$ corresponding to a horizon radius of $\delta = D/50$.

To ensure that the aerodynamic forces driving the structural fracture are accurately captured, we explicitly extracted the aerodynamic pressure at the BM points following the numerical procedure described in Section 3.3.5. These distributions were compared with the experimental data from Bashkin [64]. As shown in Fig. 18, the calculated pressure profiles along the cylinder surface are in excellent agreement with the benchmark results. This quantitative consistency is further supported by the data in Table 4, which summarizes the drag coefficients obtained from the three mesh scales alongside experimental values. The close match between the numerical and experimental results confirms that the fluid-induced forces, which serve as the primary drivers for the subsequent structural fracture in the PD module, are accurately captured.

Subsequently, an m-convergence study is conducted to examine whether the discrete PD equations adequately represent the non-local integral model. In this study, the horizon size is kept fixed while the particle spacing Δx_s is refined, so that more neighbor particles are included within the horizon as $m = \delta/\Delta x_s$ increases. Specifically, the nominal horizon size is fixed as $\delta = 0.02D$, and the particle spacing is successively refined as $\Delta x_s = D/100, D/200$, and $D/400$. The corresponding nominal horizon ratios are $m = 2, 4$, and 8, respectively. To avoid material points lying exactly on the horizon boundary, the actual horizon ratios used in the computations are slightly shifted to $m = 2.015, 4.015$, and 8.015, respectively. The resulting perturbation of the actual horizon size is only $0.015\Delta x_s$, which decreases with mesh refinement. Fig. 19 compares the vertical displacement v along the cylinder's vertical centerline at step 1700, a stage where the cracks have not yet undergone significant propagation. It is observed that the displacement profile for $m = 2.015$ exhibits a slight discrepancy compared to the finer cases, which can be attributed to the lower integration accuracy with fewer neighbor particles. However, the profiles for $m = 4.015$ and $m = 8.015$ show an excellent agreement, indicating that the basic elastic response becomes stable as the horizon is sufficiently populated. As illustrated in Fig. 20, the crack trajectory obtained with the coarsest resolution ($m = 2.015$) significantly deviates from the other cases. However, the paths for $m = 4.015$ and $m = 8.015$ exhibit excellent agreement, demonstrating that the fracture patterns have reached a converged state. Specifically, for the converged cases, the onset of crack bifurcation is observed at approximately step 7400, at a radial distance of roughly $0.38D$ from the cylinder center. This suggests that while a low horizon ratio may capture the global deformation with minor errors during the pre-fracture stage, a larger $m \geq 4.015$ is essential to accurately predict the subsequent crack path. Consequently, a horizon ratio of $m = 4.015$ is considered sufficient to accurately capture the characteristic crack propagation without compromising computational efficiency.

Finally, we perform a δ-convergence study where both the particle spacing and the horizon radius are reduced simultaneously, maintaining a constant horizon ratio $m = 4.015$. The critical stretch s_c also changes with a decreasing horizon, as defined in Eq. (18). The consistency of the structural deformation is first verified in Fig. 21, which

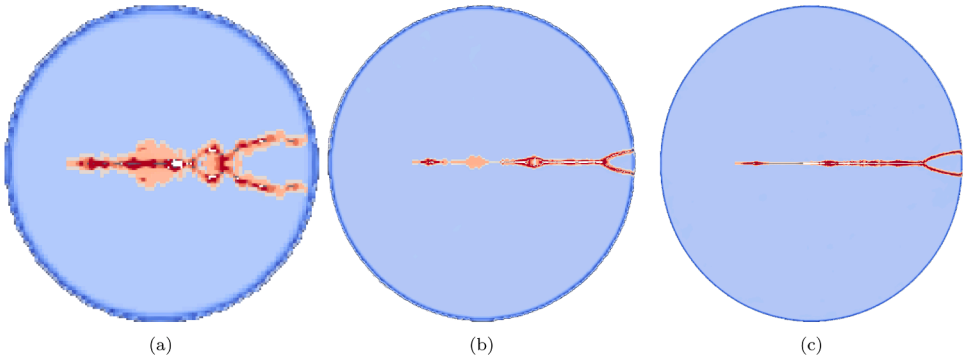

Fig. 22. Crack path computed with differentgrids for $m = 4.015$. (a)$\delta = 0.04015D$, $\Delta x_s = D/100$; (b)$\delta = 0.020075D$, $\Delta x_s = D/200$, (c)$\delta = 0.0100375D$, $\Delta x_s = D/400$.

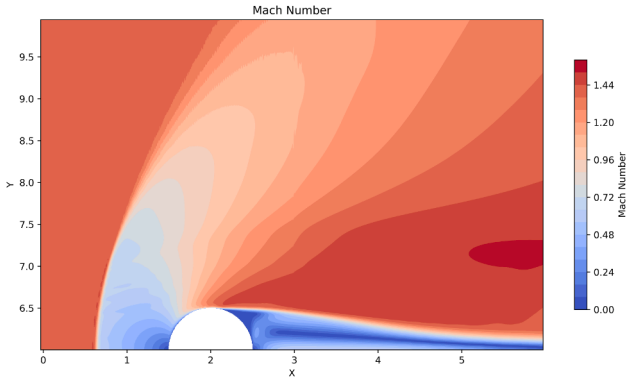

Fig. 23. Mach number distribution in the flow field around the cylinder.

plots the displacement profiles at step 1700 for the three scales. These profiles exhibit an almost perfect overlap, indicating a converged macroscopic elastic field. Nevertheless, the fracture patterns in Fig. 22 reveal that the $\Delta x_s = D/100$ case still shows noticeable discrepancies in the late-stage crack morphology. As the grid is refined to $\Delta x_s = D/200$ and $\Delta x_s = D/400$, a clear convergence in crack path is observed. Specifically, for the converged cases, the onset of crack bifurcation occurs at approximately step 7400, located at a radial distance of roughly $0.38D$ from the cylinder center. This demonstrates that the observed fracture patterns are inherent physical responses of the coupled system rather than numerical artifacts of a specific spatial discretization.

Considering both numerical accuracy and computational efficiency, a balanced configuration with $\Delta x_f = \Delta x_s = D/200$ and $m = 4.015$ is selected for all following simulations. The convergence tests demonstrate that this configuration is sufficient to capture accurate surface pressure distributions and stable crack propagation paths while maintaining an acceptable computational cost.

5.4.2. Crack propagation for different materials

Fig. 23 shows the Mach number distribution around the upper half of the cylinder. Fig. 24 illustrates crack propagation inside the cylinder under flow impact for different values of Young's modulus. As the structural response is driven by the asymmetric aerodynamic loading, the initial crack exhibits asymmetric propagation toward both the left and right sides of the cylinder. Specifically, the crack branches extending to the left remain relatively short, while the rightward-propagating cracks show more complex dynamic behavior. For the cases with lower Young's modulus (Fig. 24(a)–(c)), the rightward-propagating crack bifurcates. As the Young's modulus decreases, the crack bifurcation occurs at an earlier stage. In contrast, for the stiffest case shown in Fig. 24(d), the crack propagates along a stable path without branching throughout the simulation period.

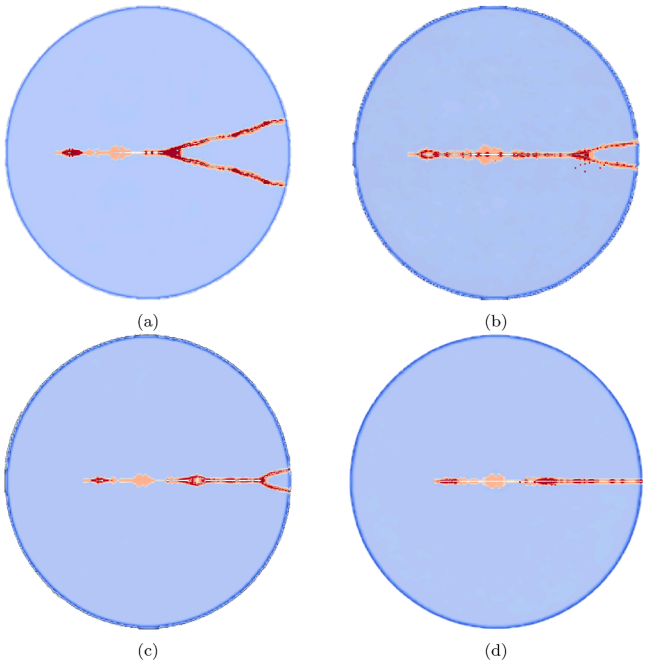

Fig. 24. Fracture in the cylinder induced by a supersonic flow. The cylinders in (a), (b), (c), and (d) have the Young's modulus of 15 MPa, 20 MPa, 25 MPa, and 30 MPa, respectively.

The results of numerical experiments show that different flow properties and physical parameters are decisive for the mode and rate of crack extension. This fully justifies the need to develop coupled flow-solid solvers that can be applied to fracture mechanics.

6. Conclusion

In this work, we present a novel hybrid algorithm that seamlessly couples compressible fluid mechanics with deformable material behavior within a unified mesoscopic framework. The gas-kinetic scheme and bond-based peridynamics are utilized to characterize the dynamics of fluids and solids, respectively. The integration of these two methods via the ghost-cell immersed boundary method facilitates a synchronized evolution of both fluid and solid fields.

The extensive numerical experiments, including subsonic and supersonic flows around canonical geometries, crack propagation, and shock wave impacts on elastic panels, demonstrate the algorithm's efficacy and its ability to predict the deformation, damage, and fracture of materials caused by high-speed flows. These results underscore the method's potential to address challenging fluid-structure interaction problems that are difficult to solve with the traditional approaches.

Looking ahead, several enhancements are envisioned to further mature this hybrid framework. A primary focus will be the implementation of a dynamic boundary reconstruction algorithm. While the current model accurately synchronizes the fluid-solid interface during global deformation, it does not yet dynamically update the topology of boundary markers to account for new surfaces generated by crack propagation. Future iterations will aim to automatically insert markers at fractured bonds, enabling the solver to capture complex phenomena such as high-speed fluid penetration into crack gaps and the resulting internal pressurization effects. Furthermore, investigations will focus on extending this framework to three-dimensional thermal interactions between fluids and structures, refining computational efficiency through adaptive mesh and time-stepping strategies, and incorporating additional physical effects to broaden the model's applicability. Overall, the proposed method represents a significant step forward in the simulation of coupled fluid and solid dynamics, offering a powerful tool for both fundamental research and engineering applications.

Computer code availability

The source code for the proposed FSI solver, along with the input files in Section 5, is open-source and available via GitHub at https://github.com/CFDML/Implementation-of-GKS-IBM-PD.

CRediT authorship contribution statement

Mingshuo Han: Writing – original draft, Visualization, Validation, Investigation, Formal analysis, Data curation; **Shiwei Hu:** Writing – original draft, Visualization, Validation, Software, Methodology, Investigation, Formal analysis, Data curation; **Tianbai Xiao:** Writing – review & editing, Writing – original draft, Supervision, Software, Resources, Project administration, Methodology, Funding acquisition, Formal analysis, Conceptualization; **Yonghao Zhang:** Writing – review & editing, Resources, Project administration, Funding acquisition, Conceptualization.

Declaration of competing interest

The authors declare that they have no known competing financial interests or personal relationships that could have appeared to influence the work reported in this paper.

Acknowledgment

The current research is funded by Strategic Priority Research Program of Chinese Academy of Sciences (XDB0620403), Chinese Academy of Sciences Project for Young Scientists in Basic Research (YSBR-107), and National Science Foundation of China (No. 12302381, 12572340). The computing resources provided by Hefei Advanced Computing Center are acknowledged.

Data availability

Data will be made available on request.

References

[1] D. Sziroczak, H. Smith, A review of design issues specific to hypersonic flight vehicles, Prog. Aerosp. Sci. 84 (2016) 1–28.
[2] E.H. Dowell, K.C. Hall, Modeling of fluid-structure interaction, Annu. Rev. Fluid Mech. 33 (Volume 33, 2001) (2001) 445–490.
[3] R. Kamakoti, W. Shyy, Fluid–structure interaction for aeroelastic applications, Prog. Aerosp. Sci. 40 (8) (2004) 535–558.
[4] M. Souli, D.J. Benson, Arbitrary Lagrangian Eulerian and fluid-structure interaction: numerical simulation, John Wiley & Sons, 2013.
[5] T.E. Tezduyar, S. Sathe, J. Pausewang, M. Schwaab, J. Christopher, J. Crabtree, Interface projection techniques for fluid–structure interaction modeling with moving-mesh methods, Comput. Mech. 43 (2008) 39–49.
[6] R. Verzicco, Immersed boundary methods: historical perspective and future outlook, Annu. Rev. Fluid Mech. 55 (1) (2023) 129–155.
[7] F. Sotiropoulos, X. Yang, Immersed boundary methods for simulating fluid–structure interaction, Prog. Aerosp. Sci. 65 (2014) 1–21.
[8] R. Mittal, J.H. Seo, Origin and evolution of immersed boundary methods in computational fluid dynamics, Phys. Rev. Fluids 8 (2023) 100501.
[9] B. Kallemov, A. Bhalla, B. Griffith, A. Donev, An immersed boundary method for rigid bodies, Commun. Appl. Math. Comput. Sci. 11 (1) (2016) 79–141.
[10] C.-C. Liao, Y.-W. Chang, C.-A. Lin, J. McDonough, Simulating flows with moving rigid boundary using immersed-boundary method, Comput. Fluids 39 (1) (2010) 152–167.
[11] Y. Kim, C.S. Peskin, A penalty immersed boundary method for a rigid body in fluid, Phys. Fluids 28 (3) (2016) 033603.
[12] S.-W. Su, M.-C. Lai, C.-A. Lin, An immersed boundary technique for simulating complex flows with rigid boundary, Comput. Fluids 36 (2) (2007) 313–324.
[13] W.-X. Huang, C.B. Chang, H.J. Sung, An improved penalty immersed boundary method for fluid–flexible body interaction, J. Comput. Phys. 230 (12) (2011) 5061–5079.
[14] A. Gilmanov, F. Sotiropoulos, A hybrid cartesian/immersed boundary method for simulating flows with 3D, geometrically complex, moving bodies, J. Comput. Phys. 207 (2) (2005) 457–492.
[15] J. Favier, A. Revell, A. Pinelli, A lattice Boltzmann–immersed boundary method to simulate the fluid interaction with moving and slender flexible objects, J. Comput. Phys. 261 (2014) 145–161.
[16] I. Lee, H. Choi, A discrete-forcing immersed boundary method for the fluid–structure interaction of an elastic slender body, J. Comput. Phys. 280 (2015) 529–546.
[17] J.-I. Choi, R.C. Oberoi, J.R. Edwards, J.A. Rosati, An immersed boundary method for complex incompressible flows, J. Comput. Phys. 224 (2) (2007) 757–784.
[18] X. Yang, X. Zhang, Z. Li, G.-W. He, A smoothing technique for discrete delta functions with application to immersed boundary method in moving boundary simulations, J. Comput. Phys. 228 (20) (2009) 7821–7836.
[19] D. Xu, J. Liu, Y. Wu, C. Ji, A high-efficiency discretized immersed boundary method for moving boundaries in incompressible flows, Sci. Rep. 13 (1) (2023) 1699.
[20] M.H.A. Azis, F. Evrard, B. van Wachem, An immersed boundary method for incompressible flows in complex domains, J. Comput. Phys. 378 (2019) 770–795.
[21] S. Dutta, C.S. Jog, A monolithic arbitrary Lagrangian–Eulerian-based finite element strategy for fluid–structure interaction problems involving a compressible fluid, Int. J. Numer. Methods Eng. 122 (21) (2021) 6037–6102.
[22] F.-B. Tian, H. Dai, H. Luo, J.F. Doyle, B. Rousseau, Fluid–structure interaction involving large deformations: 3D simulations and applications to biological systems, J. Comput. Phys. 258 (2014) 451–469.
[23] F.D. Vanna, F. Picano, E. Benini, A sharp-interface immersed boundary method for moving objects in compressible viscous flows, Comput. Fluids 201 (2020) 104415.
[24] R. Ghias, R. Mittal, H. Dong, A sharp interface immersed boundary method for compressible viscous flows, J. Comput. Phys. 225 (1) (2007) 528–553.
[25] J. Ning, H. Zhang, X. Xu, T. Ma, A novel fluid-structure interaction algorithm for compressible flows and deformable structures, J. Comput. Phys. 426 (2021) 109921.
[26] L. Wang, J. Young, F.-B. Tian, An immersed boundary method for the thermo–fluid–structure interaction in rarefied gas flows, Phys. Fluids 36 (1) (2024) 013616.
[27] A. Shahani, M.A. Fasakhodi, Finite element analysis of dynamic crack propagation using remeshing technique, Mater. Des. 30 (4) (2009) 1032–1041.
[28] L. Ramalho, J. Belinha, R. Campilho, A novel robust remeshing finite element technique for fracture propagation, Int. J. Comput. Methods 18 (02) (2021) 2050040.
[29] N. Moes, J. Dolbow, T. Belytschko, A finite element method for crack growth without remeshing, Int. J. Numer. Methods Eng. 46 (1) (1999) 131–150.
[30] T. Fries, Overview and comparison of different variants of the XFEM, Pamm 14 (1) (2014) 27–30.
[31] S.A. Silling, Reformulation of elasticity theory for discontinuities and long-range forces, J. Mech. Phys. Solids 48 (1) (2000) 175–209.
[32] S.A. Silling, M. Epton, O. Weckner, J. Xu, E. Askari, Peridynamic states and constitutive modeling, J. Elast. 88 (2) (2007) 151–184.
[33] Y. Zhang, G. Pan, Y. Zhang, S. Haeri, A multi-physics peridynamics-DEM-IB-CLBM framework for the prediction of erosive impact of solid particles in viscous fluids, Comput. Methods Appl. Mech. Eng. 352 (2019) 675–690.
[34] S. Oterkus, E. Madenci, A. Agwai, Fully coupled peridynamic thermomechanics, J. Mech. Phys. Solids 64 (1) (2014) 1–23.
[35] E. Madenci, E. Oterkus, Peridynamic Theory and Its Applications, Vol. 9781461484653 of *Peridynamic Theory and Its Applications*, Springer New York, NY, 2014.
[36] H. Zhang, D. Huang, X. Zhang, Peridynamic modeling of elastic-plastic ductile fracture, Comput. Methods Appl. Mech. Eng. 418 (2024) 116560.
[37] D. Yang, X. He, Y. Deng, An effective correspondence-based peridynamics-FEM coupling model for brittle fracture, Int. J. Mech. Sci. 264 (2024) 108815.
[38] H. Wang, L. Wu, J. Guo, C. Yu, Y. Li, Y. Wu, Three-dimensional modeling and analysis of anisotropic materials with quasi-static deformation and dynamic fracture in non-ordinary state-based peridynamics, Appl. Math. Model. 125 (2024) 625–648.
[39] L. Zhou, S. Zhu, Z. Zhu, Cosserat ordinary state-based peridynamic model and numerical simulation of rock fracture, Comput. Geotech. 155 (2023) 105240.
[40] Z. Yang, S. Zheng, F. Han, J. Cui, An efficient peridynamics-based statistical multiscale method for fracture in composite structures, Int. J. Mech. Sci. 259 (2023) 108611.
[41] S. Jafarzadeh, F. Mousavi, A. Larios, F. Bobaru, A general and fast convolution-based method for peridynamics: applications to elasticity and brittle fracture, Comput. Methods Appl. Mech. Eng. 392 (2022) 114666.

[42] D.A. Abdoh, B.B. Yin, V.K.R. Kodur, K.M. Liew, Computationally efficient and effective peridynamic model for cracks and fractures in homogeneous and heterogeneous materials, Comput. Methods Appl. Mech. Eng. 399 (2022) 115318.
[43] J.M. Zhan, X.H. Yao, F. Han, An approach of peridynamic modeling associated with molecular dynamics for fracture simulation of particle reinforced metal matrix composites, Compos. Struct. 250 (2020) 112613.
[44] S. Hu, T. Xiao, M. Han, Z. Li, E. Oterkus, S. Oterkus, Y. Zhang, An efficient explicit-implicit adaptive method for peridynamic modelling of quasi-static fracture formation and evolution, arXiv:2410.12552 (2024).
[45] M. Behzadinasab, G. Moutsanidis, N. Trask, J.T. Foster, Y. Bazilevs, Coupling of IGA and peridynamics for air-blast fluid-structure interaction using an immersed approach, Forces Mech. 4 (2021) 100045.
[46] S. Shende, M. Behzadinasab, G. Moutsanidis, Y. Bazilevs, Simulating air blast on concrete structures using the volumetric penalty coupling of isogeometric analysis and peridynamics, Math. Models Methods Appl. Sci. 32 (12) (2022) 2477–2496.
[47] K.H. Kim, A.P.S. Bhalla, B.E. Griffith, An immersed peridynamics model of fluid-structure interaction accounting for material damage and failure, J. Comput. Phys. 493 (2023) 112466.
[48] Y. Zhang, S. Haeri, G. Pan, Y. Zhang, Strongly coupled peridynamic and lattice Boltzmann models using immersed boundary method for flow-induced structural deformation and fracture, J. Comput. Phys. 435 (2021) 110267.
[49] K. Xu, A gas-kinetic BGK scheme for the Navier–Stokes equations and its connection with artificial dissipation and godunov method, J. Comput. Phys. 171 (1) (2001) 289–335.
[50] S. Chen, K. Xu, Z. Li, Cartesian grid method for gas kinetic scheme on irregular geometries, J. Comput. Phys. 326 (2016) 862–877.
[51] T. Xiao, C. Liu, K. Xu, Q. Cai, A velocity-space adaptive unified gas kinetic scheme for continuum and rarefied flows, J. Comput. Phys. 415 (2020) 109535.
[52] P.L. Bhatnagar, E.P. Gross, M. Krook, A model for collision processes in gases. I. Small amplitude processes in charged and neutral one-component systems, Phys. Rev. 94 (3) (1954) 511.
[53] E.M. Shakhov, Generalization of the Krook kinetic relaxation equation, Fluid Dyn. 3 (5) (1968) 95–96.
[54] Holway, Jr, H. Lowell, New statistical models for kinetic theory: methods of construction, Phys. Fluids 9 (9) (1966) 1658–1673.
[55] K. Xu, Direct Modeling for Computational Fluid Dynamics: Construction and Application of Unified Gas-Kinetic Schemes, Vol. 4, World Scientific, 2014.
[56] T. Xiao, A flux reconstruction kinetic scheme for the Boltzmann equation, J. Comput. Phys. 447 (2021) 110689.
[57] T. Xiao, Kinetic. jl: a portable finite volume toolbox for scientific and neural computing, J. Open Source Softw. 6 (62) (2021) 3060.
[58] S. Oterkus, E. Madenci, Peridynamic modeling of fuel pellet cracking, Eng. Fract. Mech. 176 (2017) 23–37.
[59] Y. Sun, Z.J. Wang, Y. Liu, Spectral (finite) volume method for conservation laws on unstructured grids VI: extension to viscous flow, J. Comput. Phys. 215 (1) (2006) 41–58.
[60] K. Luo, C. Mao, Z. Zhuang, J. Fan, N.E.L. Haugen, A ghost-cell immersed boundary method for the simulations of heat transfer in compressible flows under different boundary conditions part-II: complex geometries, Int. J. Heat Mass Transf. 104 (2017) 98–111.
[61] S. Takahashi, T. Nonomura, K. Fukuda, A numerical scheme based on an immersed boundary method for compressible turbulent flows with shocks: application to two-dimensional flows around cylinders, J. Appl. Math. 2014 (1) (2014) 252478.
[62] E. Madenci, E. Oterkus, Nonimpact problems, in: Peridynamic Theory and Its Applications, Springer New York, New York, NY, 2014, pp. 171–180.
[63] J. Giordano, G. Jourdan, Y. Burtschell, M. Medale, D.E. Zeitoun, L. Houas, Shock wave impacts on deforming panel, an application of fluid-structure interaction, Shock Waves 14 (1) (2005) 103–110.
[64] V.A. Bashkin, A.V. Vaganov, I.V. Egorov, D.V. Ivanov, I.S. Karas'kova, Comparison of calculated and experimental data on supersonic flow past a circular cylinder, Fluid Dyn. 37 (3) (2002) 473–483.